Observations of gravity wave refraction and its causes and consequences

Markus Geldenhuys[1], Bernd Kaifler[2], Peter Preusse[1], Joern Ungermann[1], Peter Alexander[3], Lukas Krasauskas[1], Sebastian Rhode[1], Wolfgang Woiwode[4], Manfred Ern[1], Markus Rapp[2], and Martin Riese[1]

[1]Forschungszentrum Jülich, Institute of Energy- and Climate Research, Stratosphere (IEK-7), Jülich, Germany
[2]Deutsches Zentrum für Luft- und Raumfahrt, Institut für Physik der Atmosphäre, Oberpfaffenhofen, Germany
[3]Instituto de Fısica de Buenos Aires, CONICET, Buenos Aires, Argentina
[4]Karlsruhe Institute of Technology, Institute of Meteorology and Climate Research, Karlsruhe, Germany

November 23, 2022

Abstract

Horizontal gravity wave (GW) refraction was observed around the Andes and Drake Pas- sage during the SouthTRAC campaign. GWs interact with the background wind through refraction and dissipation. This interaction helps to drive mid-atmospheric circulations and slows down the polar vortex by taking GW momentum flux from one location to an- other. The SouthTRAC campaign was composed to gain improved understanding of the propagation and dissipation of GWs. This study uses observational data from this cam- paign collected by the German research aircraft on 12 September 2019. During the cam- paign a minor sudden stratospheric warming in the Southern Hemisphere occurred, which heavily influenced GW propagation and refraction and thus also the location and amount of GW momentum flux deposition. Observations include, amongst others, measurements from below the aircraft by GLORIA (Gimballed Limb Observer for Radiance Imaging of the Atmosphere), and above the aircraft by ALIMA (Airborne Lidar for the Middle Atmosphere). Refraction is identified in two different GW packets as low as [?]4 km and as high as 58 km. One GW packet of orographic origin and one of non-orographic ori- gin is used to investigate refraction. Observations are supplemented by the Gravity-wave Regional Or Global Ray Tracer (GROGRAT), a simplified mountain wave model, ERA5 data and high-resolution (3 km) WRF data. Contrary to some previous studies we find that refraction makes a noteworthy contribution in the amount and the location of GW momentum flux deposition. This case study highlights the importance of refraction and provides compelling arguments that models should account for this.

Observations of gravity wave refraction and its causes and consequences

M. Geldenhuys[1,2], B. Kaifler[3], P. Preusse[1], J. Ungermann[1,4], P. Alexander[5], L. Krasauskas[1], S. Rhode[1], W. Woiwode[6], M. Ern[1], M. Rapp[3], and M. Riese[1]

[1]Forschungszentrum Jülich, Institute of Energy- and Climate Research, Stratosphere (IEK-7), Jülich, Germany
[2]South African Weather Service, Private Bag X097, Pretoria 0001, South Africa
[3]Deutsches Zentrum für Luft- und Raumfahrt, Institut für Physik der Atmosphäre, Oberpfaffenhofen, Germany
[4]JARA, Forschungszentrum Jülich GmbH, Jülich, Germany
[5]Instituto de Física de Buenos Aires, CONICET, Buenos Aires, Argentina
[6]Karlsruhe Institute of Technology, Institute of Meteorology and Climate Research, Karlsruhe, Germany

Key Points:

- A case study reveals that refraction results in a 25% increase in gravity wave momentum flux
- Refraction results in gravity wave momentum flux deposition at different locations
- Refraction is prominent in strong wind gradients (i.e. weak vortex conditions)

Corresponding author: Markus Geldenhuys, `m.geldenhuys@fz-juelich.de`, `markusgeld@gmail.com`

Abstract

Horizontal gravity wave (GW) refraction was observed around the Andes and Drake Passage during the SouthTRAC campaign. GWs interact with the background wind through refraction and dissipation. This interaction helps to drive mid-atmospheric circulations and slows down the polar vortex by taking GW momentum flux from one location to another. The SouthTRAC campaign was composed to gain improved understanding of the propagation and dissipation of GWs. This study uses observational data from this campaign collected by the German research aircraft on 12 September 2019. During the campaign a minor sudden stratospheric warming in the Southern Hemisphere occurred, which heavily influenced GW propagation and refraction and thus also the location and amount of GW momentum flux deposition. Observations include, amongst others, measurements from below the aircraft by GLORIA (Gimballed Limb Observer for Radiance Imaging of the Atmosphere), and above the aircraft by ALIMA (Airborne Lidar for the Middle Atmosphere). Refraction is identified in two different GW packets as low as ≈4 km and as high as 58 km. One GW packet of orographic origin and one of non-orographic origin is used to investigate refraction. Observations are supplemented by the Gravity-wave Regional Or Global Ray Tracer (GROGRAT), a simplified mountain wave model, ERA5 data and high-resolution (3 km) WRF data. Contrary to some previous studies we find that refraction makes a noteworthy contribution in the amount and the location of GW momentum flux deposition. This case study highlights the importance of refraction and provides compelling arguments that models should account for this.

1 Introduction

Gravity wave (GW) momentum flux (GWMF) and its distribution recently became a subject of debate (e.g. McLandress et al., 2012; Geller et al., 2013; Ern et al., 2017; Garcia et al., 2017; Plougonven et al., 2020; Hindley et al., 2020). At formation, the GW takes energy from the mean flow and obtains a GWMF, which, changes with wave dissipation (Plougonven et al., 2020) and refraction (Hasha et al., 2008). Refraction in the horizontal is the process whereby a GW phase front changes in orientation. Such changes in orientation are linked with changes in the wavelength in the x- and y-direction (Durran, 2009), which has been shown to have important implications for GW propagation (e.g Sato et al., 2009; Ehard et al., 2017). A literature survey shows a very small amount of papers on GW refraction compared to GW dissipation and GW breaking. This indicates that a large portion of the academic effort does not include refraction. This article uses high-resolution observational data from lower troposphere to lower mesosphere to quantify refraction and show the importance there-of for wave-mean flow interaction.

Gravity waves exist throughout the atmosphere, throughout time and virtually on all scales (Fritts & Alexander, 2003). The larger part of the GW spectrum (>50 km) helps drive stratospheric and mesospheric circulations (Holton, 2004). The slow down of the stratospheric polar vortex is also affected by GWs (Fritts & Alexander, 2003, and references there-in). These two processes affect surface weather over timescales from a few weeks to years (e.g. Kidston et al., 2015; Polichtchouk et al., 2018; Lim et al., 2019). These GWs affect the mean flow by taking momentum flux from one location to deposit at another (McLandress, 1998; Alexander et al., 2010).

Models heavily rely on parameterisation schemes to achieve a meaningful GWMF. A GW with a long horizontal wavelength can propagate large horizontal distances from its source (Krisch et al., 2017; Geldenhuys et al., 2021). Modelling this requires complex physics and processes to represent the GW drag amount and location (Plougonven et al., 2020). However, models need to simplify this due to computational constraints and confine all non-resolved GWs to their source column parameterisation schemes. The single column simplification is likely one of the causes for the disagreement between model results and observations.

The disagreement between observations and models has created a debate amongst the scientific community (e.g. McLandress et al., 2012; de la Camara et al., 2016; Garcia et al., 2017). McLandress et al. (2012) compared model to reanalysis data and found a large amount of GWMF missing at 60°S. This is a direct result of the limitation imposed in the models on the horizontal propagation of GWs. This triggered a number of studies; some reviewed parameterisation schemes (e.g. Plougonven et al., 2020; Geldenhuys, 2022), some increased drag from other known sources (e.g. Richter et al., 2010; Garcia et al., 2017; Polichtchouk et al., 2018), some studies mention islands might be the source (e.g. McLandress et al., 2012), some looked at new sources (e.g. Geldenhuys et al., 2021; Doernbrack et al., 2021) and others used GW intermittency to show increased drag (e.g. de la Camara et al., 2014, 2016). The large number of different studies to solve one problem points to the community being uncertain what the solution is or that there are a number of improvements required to our model parameterisation schemes or in our understanding.

Model reliance on parameterisation schemes is reduced with increases in spatial resolution, but for the immediate future we will still need parameterisation schemes. One of the widely used reanalysis datasets (ERA5 — European Centre for Medium-Range Weather Forecasts (ECMWF) Reanalysis 5th Generation) deposits more than double the parameterised GW drag compared to resolved GW drag during vortex breakdown (Gupta et al., 2021). Most climate models have resolutions one order of magnitude less than ERA5 data (which has a grid spacing of 0.3°), thus we can expect a greater amount of parameterised GW drag in them. Recently IFS (the underlying model of ERA5) doubled their vertical resolution and still the model required a GW parameterisation scheme (Lang et al., 2021). This shows how much we rely on parameterisation schemes. Dedicated studies (e.g. Plougonven et al., 2020; Geldenhuys, 2022) and the large effort by the modelling community (e.g. Sandu et al., 2016; Polichtchouk et al., 2018; Kim et al., 2021; Boeloeni et al., 2021) show that parameterisations are still important even though computational developments allow to resolve larger parts of the GW spectrum.

Recently Plougonven et al. (2020) stated that improved knowledge and developments in models are required for processes like GW breaking and lateral propagation. Our study suggests that refraction should be added to this list. A GW packet propagates roughly along its phase fronts (Holton, 2004), this implies the orientation and therefore the refraction of the phase fronts are important (Krisch et al., 2017). Additionally, refraction is known to increase or decrease the GWMF of a GW packet (Chen et al., 2005; Hasha et al., 2008), which is another factor not incorporated into the single column model approach. This poses the curious question of why the community is not spending more effort on refraction. One reason can be that Hasha et al. (2008) concluded that GWMF from mid-frequency waves changes due to refraction and horizontal propagation is negligible. However, they explicitly stated that a large shortcoming of their study was that they ignored non-orographic GWs and used a low model resolution (T47, or about 2.5°) compared to today's standard. The study by Hasha et al. (2008) was criticised by a commentary (Durran, 2009), who referenced an earlier study of Chen et al. (2005) saying that refraction of high-frequency GWs greatly impact the GWMF on a case-by-case basis. Dunkerton (1984) showed that stationary GWs are refracted and focused into the polar night jet by meridional shear. A high-resolution modelling study by (Sato et al., 2012) showed GWs propagate meridionally towards the 60°S polar vortex — stronger wind regions. Several other studies (e.g. Preusse et al., 2002, 2009; Sato et al., 2009; Ehard et al., 2017) looked at refraction or the focusing of GWs into the jet. Sato et al. (2009) state that "reality must be confirmed" by high-resolution observations. Although Ehard et al. (2017) is an observational study which mentions refraction, no observations of refraction was possible with their single stationary lidar. Observations are required for improved understanding of refraction and to constrain the GWMF in models, with this in mind the SouthTRAC campaign was planned.

SouthTRAC was an observational campaign, which aimed at answering some of the above mentioned shortcomings. The campaign was carried out in September and November 2019 and was based at the world's GW hotspot, the Southern Andes (Rapp et al., 2021). Rio Grande in Argentina acted as a base, from where 7 flights dedicated to GWs were performed. For more information on the campaign we refer to Rapp et al. (2021). The flight discussed here was the first local science flight of the campaign and provided some of the last deep propagating GWs of this year's winter season (see Sect. 3.1 for reasons). High-resolution observations of orographic and non-orographic GWs are used to detect refraction from the troposphere to the mesosphere. The observations are combined with model data to reveal what caused the refraction. The consequences of refraction are demonstrated by multiple raytracing experiments and calculating the GWMF along the ray path.

Section 2 describes the observational data, model data and tools employed during analysis. Section 3 starts with a synoptic overview followed by a discussion of the GW observations and their sources. Section 4 deals with the causes and consequence of refraction. The final section summarises the results and highlights the importance of refraction.

2 Data and Methods

2.1 Observational Data

Observational data for this case study include data from the GLORIA and ALIMA instruments both situated onboard the HALO (German High Altitude Long Range) research aircraft. GLORIA (Gimballed Limb Observer for Radiance Imaging of the Atmosphere) can observe 3D volumes below flight altitude while ALIMA (Airborne Lidar for the Middle Atmosphere) measures vertical profiles of temperature above the aircraft.

2.1.1 GLORIA instrument and retrieval description

GLORIA is an infrared spectrometer that measures spectra between 780 to 1400 cm^{-1} (Friedl-Vallon et al., 2014; Riese et al., 2014). The instrument contains a Michelson interferometer and a 2D infrared detector array. In the setup during SouthTRAC, 48 $\times$ 128 pixels (horizontal $\times$ vertical) of the detector array were used for limb sampling. During each interferometer sweep, each pixel records a full interferogram. The interferograms are transformed to spectra, and the spectra within pixel rows are binned. The tangent point[1] generally corresponds to the maximum signal, since the weighting function of the radiation transport has a maximum here in the optically thin case. This is a consequence of the spherical measurement geometry and the exponentially decreasing atmospheric density with altitude. The tangent point generally is seen as a region of trust in our tomographic retrievals.

GLORIA (Friedl-Vallon et al., 2014; Riese et al., 2014) is located in the belly pod of HALO and looks to the right with regard to flight direction. The field of view extends 4.1° in the vertical and the gimbal frame allows the instrument to pan from right-backwards (135° to aircraft heading) to right-forwards (45°). The vertical field of view allows a viewing depth from ≈5 km to just above flight altitude. Below ≈5 km the atmosphere becomes too optically thick for infrared limb viewing measurements as the signal becomes saturated by spectral signatures of tropospheric trace gases, clouds and aerosols. The measured radiance spectra can be analysed for signals of CO_2, O_3, H_2O, NH_3, $ClONO_2$, HNO_3 and PAN — Peroxyacetyl nitrate, among others.

[1] The tangent point is the point closest to the surface of the earth where the density is the highest.

In this article we use emission lines of the CO_2 band at 936.8 – 938.6, 939.2 – 941.0 and 942.2 – 944.2 cm^{-1} to retrieve temperature. The forward model for the retrieval used a spectral resolution (of 0.2 cm^{-1}) similar to the GLORIA spectral sampling. The data presented in this article was obtained by panning the instrument from 49° to 129° in 11 steps of 8°.

The GLORIA data was processed into a 1-D retrieval and a 3-D dataset. A 1-D retrieval consists of a temperature signal that was averaged over each row of detector array for each respective line-of-sight. This produces 11 different 1-D retrievals from each of the azimuth angles. The GW perturbation was extracted from the 1-D retrieval by subtracting a smoothed ECMWF temperature, which is also the a priori of the retrieval. To obtain a 3-D dataset, tomography is required. Two types of tomography exist, full-angle and limited-angle tomography. Full-angle tomography can take place where the airmass is observed from all sides by a circular flight path (e.g. Krisch et al., 2017; Krasauskas et al., 2021). Limited-angle tomography is obtained from straight flight legs (e.g. Krisch et al., 2018; Geldenhuys et al., 2021). The panning ability allows GLORIA to observe a single airmass from different angles. This allows us to reproduce a 3-D atmosphere (for details on this please refer to e.g. Ungermann et al. (2011); Kaufmann et al. (2015); Krisch et al. (2018); Krasauskas et al. (2019)). The data was processed using the GloriPy (Kleinert et al., 2014) and JURASSIC2 (Juelich Rapid Spectral Simulation Code version 2; Ungermann et al. (2010)) software packages. Similar to Geldenhuys et al. (2021) and Krasauskas et al. (2021) the retrieval used the Laplacian regularisation with a Delaunay triangulation-based, irregular grid-capable discretisation. The GW perturbation was extracted from the 3-D retrieval by subtracting a smoothed retrieval. The smoothed retrieval was created by applying a third order polynomial smoothing in the x- and y-directions with 51 point smoothing and a fourth order polynomial in the z-direction with 11 point smoothing.

2.1.2 ALIMA - Airborne Lidar for the Middle Atmosphere

ALIMA measures the atmospheric density profile from which temperature is calculated (Rapp et al., 2021). ALIMA is an iron resonance and Rayleigh lidar, however, during the SouthTRAC campaign, only the Rayleigh lidar was installed. Within the HALO body there is an optical window, which allows ALIMA to look upwards. Under ideal conditions ALIMA measures from 2 km above flight altitude up to 80 km by Rayleigh scattering.

Measuring up to 80 km requires a strong initial pulse and multiple fine-tuned detectors. ALIMA provides an initial pulse at 532 nm and receives backscatter by a telescope 48 cm in diameter (Rapp et al., 2021). The detected backscatter has a large dynamic range. Thus, ALIMA uses three detectors with different sensitivities that are optimised for the near, mid and far region. A mechanical chopper blocks the intense backscattered light originating within 4 km above the aircraft in order to prevent overloading of the detectors. The mid and far detectors are gated relative to the opening of the chopper to avoid saturation.

Following Hauchecorne and Chanin (1980) the lidar profile from each detector is converted to a temperature profile by hydrostatic downward integration in steps of 100 m. This requires a top of profile temperature, which is taken from SABER satellite data. The top of profile temperature of the lower profiles is taken from the above profile. The three profiles are then merged into a single profile covering the whole altitude range (Kaifler & Kaifler, 2021). At the top of the profile, the error can be large, but since pressure increases exponentially downwards, the error similarly decreases exponentially downwards. The error decreases from 6.5 K above 70 km to 2.9 K between 60–70 km to 0.9 K below 60 km (Rapp et al., 2021). Temperature data used in this manuscript had a 1 min resolution, which roughly equates to ≈15 km resolution along the flight direction.

To obtain a curtain of GW perturbation, a 30 min running mean temperature is subtracted. Removing the background temperature reveals a complex GW structure exhibiting GWs of different scales and different propagation directions. Wavelet analysis was used to further analyse this complex interference pattern. Wavelet analysis has been applied to lidar data before to separate GWs of different orientations (Kaifler et al., 2017). Assuming non-stationarity on the straight flight legs a 2-D Morlet continuous wavelet transform (e.g. Torrence and Compo (1998)) was computed according to Chen and Chu (2017), using a Morlet oscillation parameter (k factor) of $^2/_\pi$. We found a discretisation starting at a spatial scale of 40 km while using 20 spatial and 30 angular scales sufficient in order to separate different slants of GW phase fronts. By making the assumption that the GWs propagate against the ERA5 reanalysis wind we determine upward and downward propagating GWs.

The 2-D Morlet continuous wavelet transform is much better equipped than the fast Fourier transform to deal with non-harmonic waves, but there are still some inherent problems visible in the derived amplitudes. An amplitude signal of an upward propagating non-harmonic GW will leak to the downward propagating GW, lowering the 'real' temperature amplitude of the upward propagating GW. For this reason, all temperature amplitudes were determined using temperature perturbation components before application of the continuous wavelet transform.

2.2 Model and Reanalysis Data

2.2.1 Mountain Wave Model

The mountain wave model is a tool to estimate mountain wave activity. Mountain wave activity is estimated by a three step process: ridge identification, GW characteristics determination, and GROGRAT raytracing. The model itself follows the original approach of Bacmeister et al. (1994), but differs in a key aspect of the ridge detection method. Briefly described, the mountain wave model reduces a given set of topography (ETOPO1 1Arc-Minute Global Relief Model (Amante & Eakins, 2009)) to a set of possible ridges by applying a Gaussian bandpass filter to single out the scales of interest and performing a probabilistic Hough transformation. This provides a lines representing possible corresponding positions, lengths and orientations of mountain ridges. Afterwards the mountain wave parameters are estimated by fitting idealised (Gaussian shaped) ridges to the bandpass filtered topography for each of these lines. From this a horizontal wavelength as well as displacement amplitude is estimated. The horizontal wavelength is determined by multiplying the ridge width by a fixed factor. The displacement amplitude reflects the height of the barrier. By passing these GW characteristics to the GROGRAT raytracer, the model can predict the time development of the mountain waves. For information regarding the background data for input into GROGRAT, see Sect. 2.2.3.

2.2.2 WRF (Weather Research and Forecasting) Model Data

A high-resolution WRF model (version 4.2) is used to fill the data gaps when validating the raytracing and ALIMA results (Sect. 3). Boundary input conditions were supplied every 6 hours at a $0.25 \times 0.25°$ resolution from the Global Data Assimilation System (GDAS) from the National Centres for Environmental Prediction (NCEP). The WRF model was nested twice to produce a 9 km and ultimately a 3 km horizontal grid point distance. Vertical resolution was 0.5 km. The data extends from the surface to 42 km with a 10 km sponge. Only data below the sponge layer (32 km) are used in this work. The model spin-up time was 1 day — only data after spin-up time was used.

To separate GWs from the background fields a 2-D Fast Fourier Transform was used. The spectrum was cut at a horizontal wavelength of 400 km, retaining all longer wavelengths in the background. The GW perturbation field formed the residual after the background field was subtracted from the actual field. Experiments with a 600 km cut-off produced similar GW perturbations.

2.2.3 Reanalysis Data

This article uses ERA5 (European Centre for Medium-Range Weather Forecasts Reanalysis 5th Generation; (Hersbach et al., 2020)) data on a 0.3° × 0.3° × 200m grid on geopotential altitudes. Only data for the synoptic discussion are on a pressure grid. To remove the GW component from the background flow a zonal Fast Fourier Transform was used with a cut-off at zonal wavenumber 12 (Strube et al., 2020), corresponding to 1900 km. This was followed by a Savitzky-Golay filter (Savitzky & Golay, 1964) in the y- and z-direction. In the meridional (y) direction a third-order polynomial with a 50 point (15°) smoothing was applied. In the remaining direction (z) a fourth-order polynomial was applied with a 15 point (3 km) smoothing. The result after smoothing produces the background conditions. Subtracting the smooth background conditions from the original field produces the GW perturbation component. The smooth background fields were visually studied to ensure no GWs signals were left in the field. The smooth background is used as input into the GROGRAT raytracer. The unfiltered horizontal divergence field is used to show the GW field.

2.3 GROGRAT – Gravity-wave Regional Or Global Ray Tracer

GROGRAT traces the propagation of a GW forward or backward in time. GROGRAT uses the dispersion relation (Marks & Eckermann, 1995; Eckermann & Marks, 1997):

$$\omega^2 = \frac{(k^2+l^2)N^2 + f^2\left(m^2 + \frac{1}{4H^2}\right)}{k^2+l^2+m^2+\frac{1}{4H^2}} \tag{1}$$

and the raytracing equations:

$$\frac{dk}{dt} = -k\frac{\partial u}{\partial x} - l\frac{\partial v}{\partial x} - \frac{1}{2\omega\Delta}\left[\frac{\partial N}{\partial x}^2 (k^2+l^2) - \frac{\partial \alpha}{\partial x}^2 (\omega^2 - f^2)\right] \tag{2}$$

$$\frac{dl}{dt} = -k\frac{\partial u}{\partial y} - l\frac{\partial v}{\partial y} - \frac{1}{2\omega\Delta}\left[\frac{\partial N}{\partial y}^2 (k^2+l^2) - \frac{\partial \alpha}{\partial y}^2 (\omega^2 - f^2)\right] - \frac{f}{\omega\Delta}\frac{\partial f}{\partial y}(m^2+\alpha^2), \tag{3}$$

where ω is intrinsic frequency, N is Brünt-Väisälä frequency, f is Coriolis frequency, H is scale height, k, l, m are wavenumbers in x, y, z - direction, u is zonal wind, v is meridional wind, $\Delta = (k^2 + l^2 + m^2 + \alpha^2)$, $\alpha = \frac{1}{2H_\rho}$, and H_ρ is density scale height. GROGRAT use these equations and ω_{gb}, k, l (where $_{\mathrm{gb}}$ indicates ground-based) and location as input to calculate the propagation path of the GW in space and time. Wave action density,

$$A \equiv \frac{\bar{E}}{\omega}, \tag{4}$$

is conserved along the ray path. Thereby $\bar{E}$, the total energy transported by the waves, is defined as

$$\bar{E} = \frac{1}{2}\rho\left(\frac{\hat{T}}{T}\right)^2\left(\frac{g}{N}\right)^2\frac{\omega^2}{\omega^2 - f^2}, \tag{5}$$

where ρ is density, g is the gravity constant, $\hat{T}$ is temperature amplitude and T is temperature. In addition, wave amplitude growth is limited by saturation amplitudes calculated using the scheme of Fritts and Rastogi (1985), while turbulent and radiative damping are considered according to Pitteway and Hines (1963) and Zhu (1993).

GROGRAT uses the smoothed ERA5 background wind, temperature, and pressure (Sect. 2.2.3) that varies in time as input into the raytracing equations. This means that the background conditions influencing the wave vector vary with every time step of ray integration. This forms the 4-D propagation setup, meaning the wave can propagate in time, latitude, longitude, and altitude direction. The propagation physics is complete as far as WKB (Wentzel-Kramers-Brillouin approximation (Marks & Eckermann, 1995; Hertzog et al., 2001)) allows and comprises in particular horizontal propagation and refraction (similar to the setup used in Krisch et al. (2017, 2020); Geldenhuys et al. (2021); Strube et al. (2021)). In this paper alternative 3-D and 1-D propagation setups are used to compare to the 4-D propagation results. The 3-D propagation setup assumes the background constant with time and uses a single snapshot to propagate the GWs. The 1-D setup represent conditions when horizontal propagation and refraction are both disabled by setting the horizontal phase speed, $\frac{dk}{dt}$ and $\frac{dl}{dt}$ (Eqs. 2 and 3) to 0. This is analogous to a 1-D parameterisation scheme employed in a general circulation model.

3 Synoptic Overview and Refraction Observation

3.1 Synoptic Situation

The research flight took off on 11 September 2019 at 23:00 UTC and landed on 12 September shortly before 07:00 UTC. All dates provided in this article pertain to the year 2019 (unless explicitly stated otherwise) and all times are in UTC. The observations discussed in this article were performed between 03:30 and 06:30 when the racetrack[2] was flown. Observations used in this article are from the long parallel legs of the racetrack (grey lines in Fig. 1). The southern leg was flown first from east-to-west followed by the northern leg from west-to-east. We choose 03:00 on 12 September to be representative for the synoptic situation of the racetrack. At 500 hPa a Rossby wave is observed over the Drake Passage (Fig. 1).

The cold front (Fig. 1) passed over Rio Grande ≈5 h before flight take-off. The cold front is situated in a well developed Rossby wave at 500 hPa. Behind the cold front cold stable air is advected onshore by a ridging high pressure system. This creates south-southwesterly flow over the southern most tip of Patagonia, veering to south-west (at 50°S), west-south-west (at 45°S) and west (at 40°S) in a northwards direction along the Andes mountain range. The stable conditions with wind flow nearly perpendicular (within 30°) across the mountains (ICAO, 2005; Geldenhuys et al., 2019) creates prime conditions for a whole spectrum of different orientation GWs entering the observation regime. The narrow mountains on the tip of Patagonia are expected to form shorter horizontal wavelengths. The broad Andes ridge to the north is expected to excite long horizontal wavelengths with possible shorter waves coming from the side ridges leading up to the main ridge (Van der Mescht & Geldenhuys, 2019). All of these GWs is expected to superimpose and create a rather complex interference pattern.

Polar stratospheric clouds formed presumably in the GWs coming from the broad main ridge. The clouds were observed in the racetrack at 23 km altitude by ALIMA (Dörnbrack et al., 2020). Enhanced backscatter from the clouds means that ALIMA temperature measurements can only be used above this altitude or need to be interpolated through the cloud layer. The polar stratospheric clouds extended unusually far north. This was attributed to a displaced stratospheric polar vortex.

The most significant event in the atmospheric region under consideration was a sudden stratospheric warming (Shen et al., 2020). This minor sudden stratospheric warming was a displacement event (Fig. 2) forced by a bottom-up mechanism: an anomalously strong wavenumber 1 activity propagating upwards from the troposphere. The strong

[2] A flight pattern consisting of two legs parallel to one another.

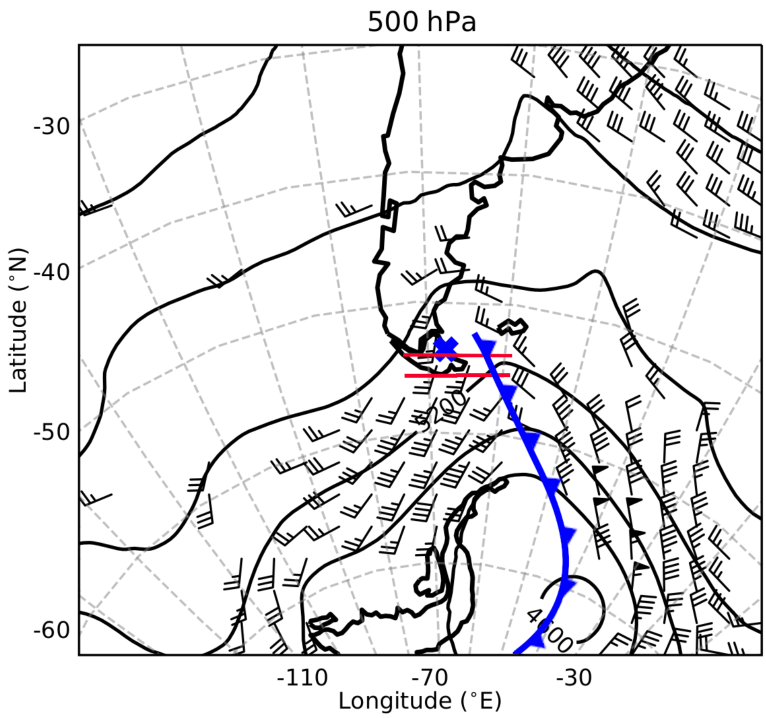

Figure 1. Synoptic situation in the mid-troposphere at 500 hPa on 12 September at 03:00 as indicated by ERA5. Black lines show geopotential height lines. Wind barbs only show wind where the total wind speed exceed $20\,\mathrm{ms}^{-1}$. A short barb indicate $5\,\mathrm{ms}^{-1}$, a long barb $10\,\mathrm{ms}^{-1}$ and a triangle $50\,\mathrm{ms}^{-1}$. Note the Rossby wave with the cold front (blue line) directly downstream of Patagonia. The blue cross indicates the take-off location (Rio Grande) and the red lines over the southern tip of South America show the parallel racetrack legs used in the GLORIA and ALIMA retrievals.

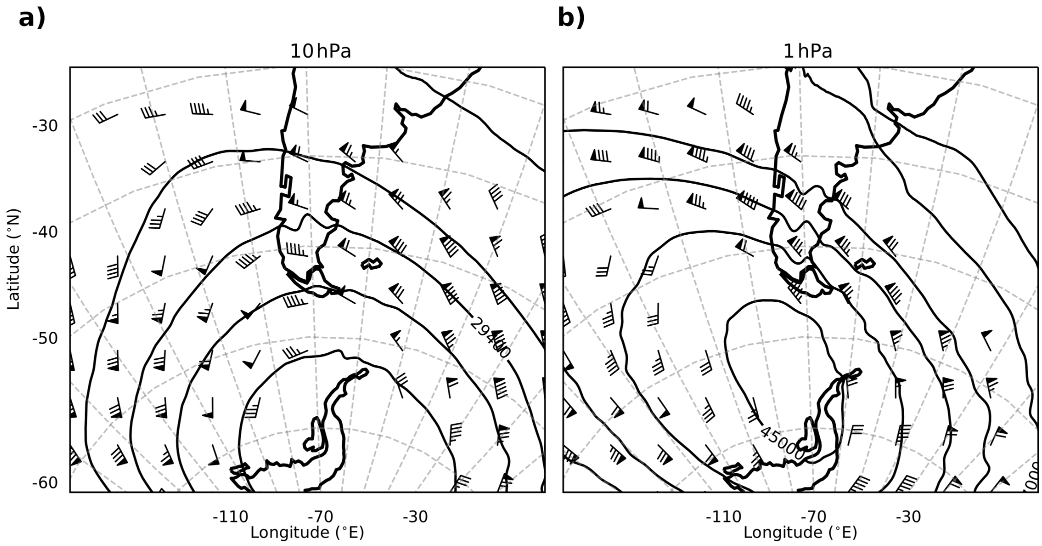

Figure 2. Stratospheric synoptic situation at 10 hPa (a) and 1 hPa (b) on 12 September at 03:00 as indicated by ERA5. Black lines and wind barbs are similar to Fig. 1. Note the displaced polar vortex with its centre located at 70°S 60°W at 10 hPa and 65°S 75°W at 1 hPa.

wavenumber 1 activity was in turn forced by anomalously strong convection over the Pacific Ocean. The sudden stratospheric warming caused a rapidly weakening polar vortex with temperatures increasing rapidly from above to below. Both the weakening in the wind and the strong change in temperature is unfavourable for GW propagation and cause GW dissipation or the trapping of GWs. Both of these act as a lid to restrict the GW activity moving upwards.

The slow down in the 10 hPa zonal average winds appeared in the first few days of September[3]. By 11th September, the slow down had merely started and still allowed GW propagation to vortex altitudes. This is confirmed by the strong westerly winds shown in ERA5 data on Figure 2. The location of the polar vortex creates a large amount of wind speed shear and directional shear. The shear is expected to form prime conditions for refraction.

3.2 GW Observations: Tropospheric and Lower Stratospheric

The viewing geometry of GLORIA allows tropospheric and lower stratospheric observations. The southern leg of the racetrack (Fig. 1) was used in the GLORIA retrieval and was flown from east to west at 13.5 km.

3.2.1 GLORIA Observations: 3-D

The 3-D GLORIA temperature field is obtained from a 3-D tomographic retrieval. The retrieval reveals short horizontal wavelength GWs in the lee of the south western most tip of Patagonia. The horizontal cut in Figure 3 shows two distinct GW orienta-

[3] Using data from MERRA-2 (Modern-Era Retrospective analysis for Research and Applications — Gelaro et al. (2017)). MERRA-2 data are used as it assimilates MLS (Microwave Limb Sounder) satellite data, which makes it a more trustworthy dataset in the upper stratosphere and lower mesosphere (Ern et al., 2021).

tions. The first is aligned west-east and the second from north-west-to-south-east. Taking the GLORIA viewing geometry into consideration we theoretically have less trust in the west-east orientated feature. The viewing angles of GLORIA are aligned across the west-east orientated phase fronts.

If the line of sight spans across a positive and a negative region, the signal will be an averaged value of the warm and cold regions. The amount that each feature contribute depends on the density. The densest part will have the most molecules, radiating the most energy. This means the warm and the cold phase fronts average out to have a weak signal, i.e. no retrievable GW. Considering this, we are tempted to classify these structures parallel to the flight path (the westernmost indicated warm front on Fig. 3) as artefacts, however, in the mountain wave model (Sect. 2.2.1) and the high-resolution WRF model (Sect. 2.2.2 and 3.2.3) this structure also exists. This adds trust to the retrieval process (and the complex physics and mathematics behind it), when the result is better than what simplified physics dictate it should be.

The second GW orientation is aligned north-west-to-south-east. Horizontal cuts at different altitudes similar to Figure 3 and a vertical cut perpendicular through the GW phase fronts reveal a horizontal wavelength of 116 km, vertical wavelength of 4.4 km, amplitude of $\approx$3 K and an orientation of 230°. Krisch et al. (2018) found that limited-angle tomography (method used to produce the 3-D retrieval while flying on straight legs) enhances the uncertainty/error of the phase front orientation. Considering that orientation is important in a refraction study, we complement the orientation results with the 1-D retrieval.

3.2.2 GLORIA Observations: 1-D

A 1-D GLORIA retrieval consists of a retrieved temperature signal for a single line-of-sight. A 1-D retrieval converts single radiance profiles into temperature profiles by assuming a horizontally homogeneous atmosphere. The 1-D data is combined along the aircraft direction of flight to create a 2-D dataset. The first dimension represents time and the second altitude. The retrieved result of each detector row average is represented by its tangent point along the line of sight. Each GLORIA viewing angle observes the GW phase front differently (Fig. 4). Where the line of sight aligns along the GW phase front a greater signal is obtained, as opposed to looking across the phase fronts at an angle. Looking across a succession of GW phase fronts dampens the wave amplitude in the observed radiance (Preusse et al., 2002). For a specific altitude the maximum temperature amplitude is reached when the line of sight and phase fronts are aligned. The viewing angle of the most pronounced signal is then used for the wave orientation with an error of half a scanning step (4°) as error estimate.

At 8 km altitude the maximum amplitude in Fig. 4 is observed for an angle of 65°. The maximum at 10 km occurs at 57° and at 12 km at 49°. Taking into account the aircraft heading of 268° and subtracting 90° to convert from phase-front orientation to wavevector, we obtain a ground-based orientation of 243° for the 65° viewing angle. Satellite data from GOES (Geostationary Operational Environmental Satellite — not shown) channel 8 to 10 indicate a GW orientation of $\approx$240° between $\approx$615 hPa ($\approx$4 km) and 340 hPa ($\approx$8 km), consistent with the lowest GLORIA altitude. Accounting for the fact that amplitudes are maximum at different altitudes for different GLORIA viewing angles, we can conclude that at higher altitudes (Fig. 4) the orientation turns anticlockwise to 235° at 10 km and $<$227° at 12 km (GLORIA has no viewing angles lower than 49°, which means the orientation can be lower than 227°). Assuming one wave packet with a fixed orientation at launch, the refraction between 8–12 km is at least 16°.

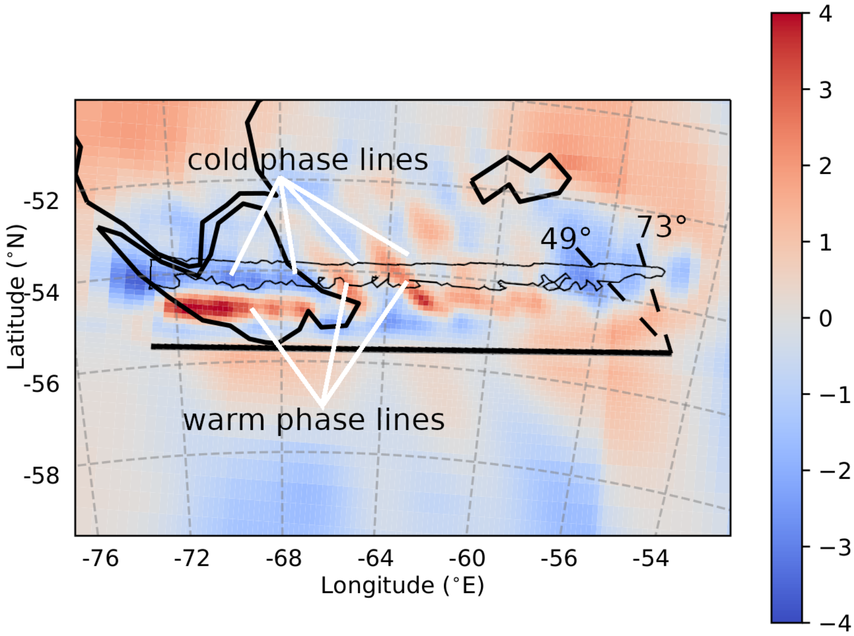

Figure 3. Temperature perturbation component at 10 km altitude of the GLORIA tomographic field. The retrieval was computed using data only from the southern leg (thick black line). Using both the northern and southern leg in a combined tomographic retrieval created artefacts due to non-symmetrical tangent point distribution. A retrieval using only the northern leg produced a GW field similar to the southern leg. Black solid lines indicate the Patagonia coastline and the straight white solid lines point to different phase fronts. The region encircled by the thin black line indicates our tangent point region for this altitude, which is our region of trust (Sect. 2.1.1). The dashed black lines indicate the maximum and minimum GLORIA line of sight angle discussed in Fig. 4.

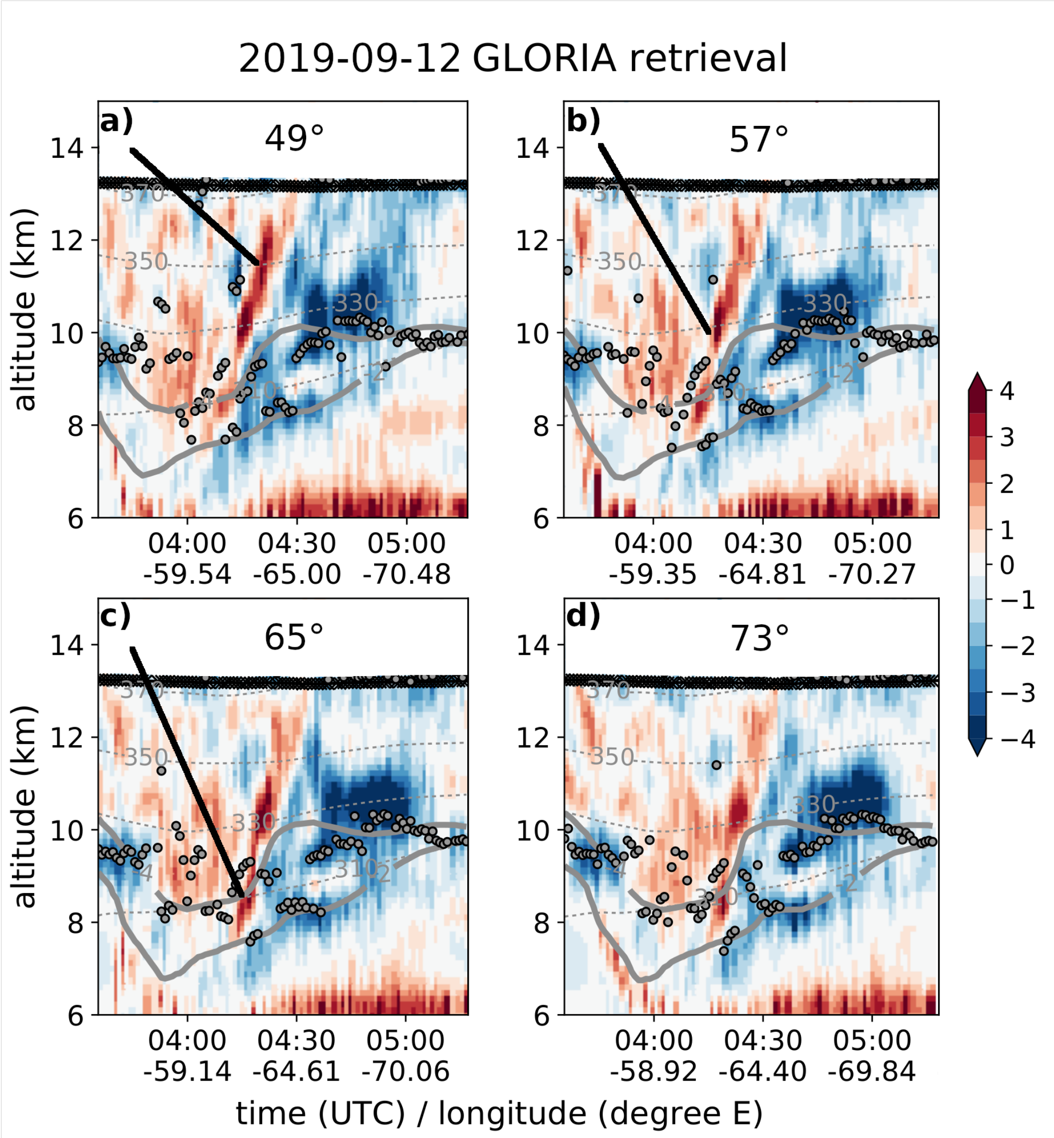

Figure 4. Temperature perturbations (in K) from GLORIA 1-D observations for 4 of the 11 azimuth angles (49°, 57°, 65°, and 73°). The angles are between the observation direction and HALO aircraft heading. Note how the maxima of the warm phase front at fixed altitudes depend on the viewing angle (marked by thick black line). Flight altitude was at 13.5 km, the thick grey lines indicate dynamic tropopause at -2 and -4 potential vorticity units and the thin dashed grey lines show potential temperature — both extracted from ECMWF analysis data. The dots indicate the suggested thermal tropopause as determined from the retrieval, however, the gravity wave signature will influence this. Data is valid for the southern leg of the racetrack and longitude values represent tangent point longitude.

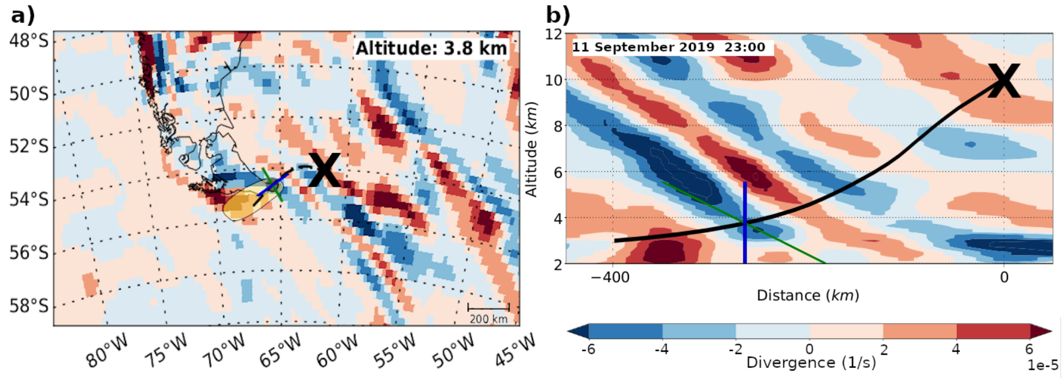

Figure 5. GROGRAT backtrace using GLORIA observations as input overlaid on horizontal wind divergence from ERA5. The raytracing starts on 12 September at 03:00 at 10 km and traces back ≈5 h. Both panels a and b are valid for 23:00, 4 h before observation. Panel a shows a horizontal cross-section with the ray as a dashed line and ERA5 divergence at 3.8 km. The yellow transparent region surrounding the end of the ray shows the spread of the ensemble members. The thin black line represents the coastline and the X the start of the ray. Panel b shows the vertical cross-section as interpolated along the ray (black line). The location of the GW packet for this respective time is indicated by the cross of the blue and green line. The blue line on the left (right) plot shows the horizontal (vertical) wavelength from the backtrace. The green line shows the phase orientation.

3.2.3 Raytracing and WRF comparison

In this section GROGRAT is checked for consistency to ALIMA and WRF before subsequent experiments are conducted (Sec. 4.2). GROGRAT requires the ground-based frequency as well as the wavelength in the x- and y (zonal and meridional) directions as input. The ground-based frequency is obtained via the dispersion relation (Eq. 1) from the observations (Sect. 3.2.1) and ERA5 background winds. To account for the measurement error the input values are perturbed by 10% to form an ensemble raytrace. Tracing the ensemble backwards in time produces a spread of rays surrounding the south coast of Patagonia (Fig. 5 — the yellow region includes all but one ensemble member (the perturbation associated with a shorter vertical wavelength propagated to 58.5°S 75.5°W and was neglected in the spread)). All ensemble members end in close vicinity in the horizontal and vertical to the coastal mountains (Fig. 5). This is a key indicator that the complex mountains on the south coast of Patagonia are the source of the GWs. GLORIA observed the GWs ≈5 h after formation. The GROGRAT suggested horizontal wavelength, vertical wavelength and phase orientation agrees well with the ERA5 data. The consistency builds trust in the features seen in observations, GROGRAT and ERA5.

The forward raytrace of the GW observed by GLORIA is compared to ALIMA for further verification. The ray remains below the ALIMA observational range and reaches ALIMA observational altitudes south of the racetrack (Fig. 6). The ray takes ≈3 h to propagate from the observation altitude to 27 km. Time wise this makes the raytrace directly comparable to the WRF data on 12 September 06:00. The ALIMA southern leg was flown east to west between 03:30 and 05:20 and hence 40 min to 2.5 h before the time the WRF model is evaluated. The comparison relies on the assumptions that the GW structure (phase and amplitude) does not alter in this time frame.

The reconstructed GROGRAT GW in Figure 6 compares well to the WRF and ALIMA data. It is noted that the eastern most part of the leg has the biggest time differ-

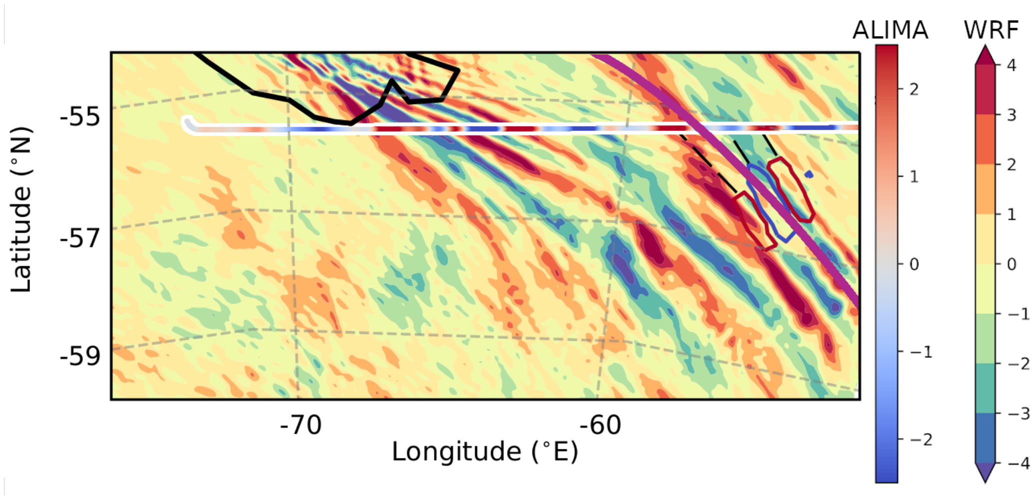

Figure 6. The forward raytrace (magenta line) of the GLORIA observed GW overlaid with WRF and ALIMA data. All data are valid for 27 km altitude. The background data is WRF data while the red and blue line with the white border represents ALIMA data on the southern flight track after the upward propagating waves were selected with a wavelet transform (Sect. 2.1.2). The red and blue contour lines show warm and cold phases of the reconstructed GROGRAT GW respectively. The reconstructed GWs and WRF data are both valid for 12 September 06:00. To guide the eye, the black-dashed lines create a link between GROGRAT reconstruction and the ALIMA track, which shows that the phase fronts of the GW match well. The plot is exclusively used to match the GW structure and validate GROGRAT versus ALIMA. Note that the temperature (in K) scale are different for WRF and ALIMA — the wavelet transform would cause the ALIMA temperature amplitude to be lower than the actual amplitude (Sect. 2.1.2).

ence between the ALIMA observation and the GROGRAT GW, hence we could expect differences. Between 62° and 68°W the WRF model and ALIMA compares remarkably well. The WRF data fills the gaps between ALIMA measurements and the reconstructed GROGRAT GW; making it a useful dataset. Using the ALIMA data by itself becomes complicated as there are many short horizontal wavelength GWs (e.g. between 62° and 68°W), which is difficult to interpret using only the two ALIMA curtains. The WRF model simulates the shorter horizontal wavelength GWs well, which makes it easier to interpret the ALIMA data.

3.3 GW Observations: Mid- and Upper Stratosphere

ALIMA provides high resolution 2-D observations above HALO. Normally, a 2-D dataset does not allow the determination of the full 3-D GW vector. Thus, on the one hand a curtain observation does have a slight disadvantage as opposed to a 3-D dataset. But on the other hand, with creative experiment design (flight planning) this is easily overcome. To infer also direction information, the racetrack was planned with two parallel flight tracks spaced less than one expected wavelength of the major GW structure. In the following discussion we use data from 04:15 to 06:05, this implies assuming a stationary environment for ≈2 h in the combined analysis. We initially assume the GW structure is stationary and test this with every GW packet we observe. The temperature perturbation field shown in Fig. 7a and b were determined by subtracting a 30 min running mean and applying a wavelet transform as specified in Section 2.1.2. Three GW families are identified in the ALIMA curtains on Figure 7a and b. The southern leg (Fig. 7a) shows two long horizontal wavelength GWs. A first wavepacket (family 1) has a top at ≈40 km and starts 32 km — with a weak signature extending down to 27 km (the GWs on Fig. 6). Compared to family 1, the phase fronts of the higher wavepacket (family 3) have a steeper slant, show a shorter horizontal wavelength and a smaller GW amplitude. The 'dead zone' (weak amplitudes and an incoherent structure) between these packets and the differences in the GW properties indicate that these are two distinct GWs. Horizontal cuts through the ALIMA data (similar to Fig. 9) show a well defined GW pattern that disappears around 40 km. This is further evidence of two GWs rather than structures of the same GW packet.

The northern leg (Fig. 7b) exhibits three dominant GW packets. The first GW packet exhibits strong similarities to family 1 (in the southern leg) in the left plot and is categorised as the same GW packet. Above family 1 (in the 'dead zone' of the southern leg in Fig. 7a) another GW packet is identified (family 2). A study by Kaifler et al. (2022) found a similar change as Fig. 7b in vertical wavelength above and below 40 km. Their study used a flight leg also from SouthTRAC flight 8, which extended from north-west to south-east across the main Andes ridge. The GW packet between 40 km and 50 km on Fig. 7b has no similarities to family 1 or 3 and is hardly discernible in the southern leg (mainly at flight distances < 700 km). This suggests that the GW packet does only weakly extend to the southern leg. With only one leg we cannot determine a 3-D wavevector for family 2. A separation between family 2 and the upper GW packet is around 50 km. The upper GW packet is clearly defined between 51 km to 60 km. This GW packet closely resembles family 3 in the southern leg (left) and is categorised accordingly. The presence of three different families hints towards three different origins.

A first attempt is made at determining the source origins with the simple mountain wave model (Sect. 2.2.1). Figure 7c and d represent the reconstructed temperature fluctuations from the mountain wave model sampled along both legs. Considering the simplifications inherent in the model only a qualitative agreement is expected. The results compare well to ALIMA observations (Figure 7a and b) of family 1. The horizontal wavelength is visibly shorter in the mountain wave model. One possible explanation for this is that the mountain wave model only uses the width of the ridge to determine the horizontal wavelength and does not take the low-level blocking width into account as suggested by Geldenhuys (2022). An interference GW structure exists (Fig. 7d) in the layer containing family 2 and only vaguely similar to the ALIMA observations. At first a structure similar to family 3 is observed in Figure 7c and d. However, closer inspection reveals a longer vertical wavelength (7.5 km in ALIMA data and up to 11.3 km in the mountain wave model) and a slower ground-based phase speed ($13\,\mathrm{ms}^{-1}$ for the ALIMA GW and $\approx 2\,\mathrm{ms}^{-1}$ for the mountain wave model GW). Other minor differences include the separation occurring at 43 km and 53 km compared to 40 km and 50 km in the observations (Fig. 7). However, the strong change in phase slant and horizontal wavelength (Fig. 7) above and below the separation compare well between model and observations (Fig. 7). The mountain wave model is a linear model and the critical layer at ≈38 km (see the GW momentum deposit discussion in Section 4.2) implies non-linearity for all GWs above this layer; and provides a possible reason for the mismatch above this layer.

Topography is the only GW source in the model indicating that family 1 stems from the Andes. Figure 8 shows the family 1 GW propagating westwards and southwards in a horizontal cut. The mountain waves propagate a significant distance from the mountains demonstrating that source attribution due to co-location is not a good approach. The GW propagating into the Drake Passage is also a possible explanation for the missing GW drag at 60°S. Further analysis into the model showed family 1 originates from the main Andes ridge at 49°S and the incoherent GWs between 40 to 50 km (Fig. 7c and d) originate from ridges north of 49°S.

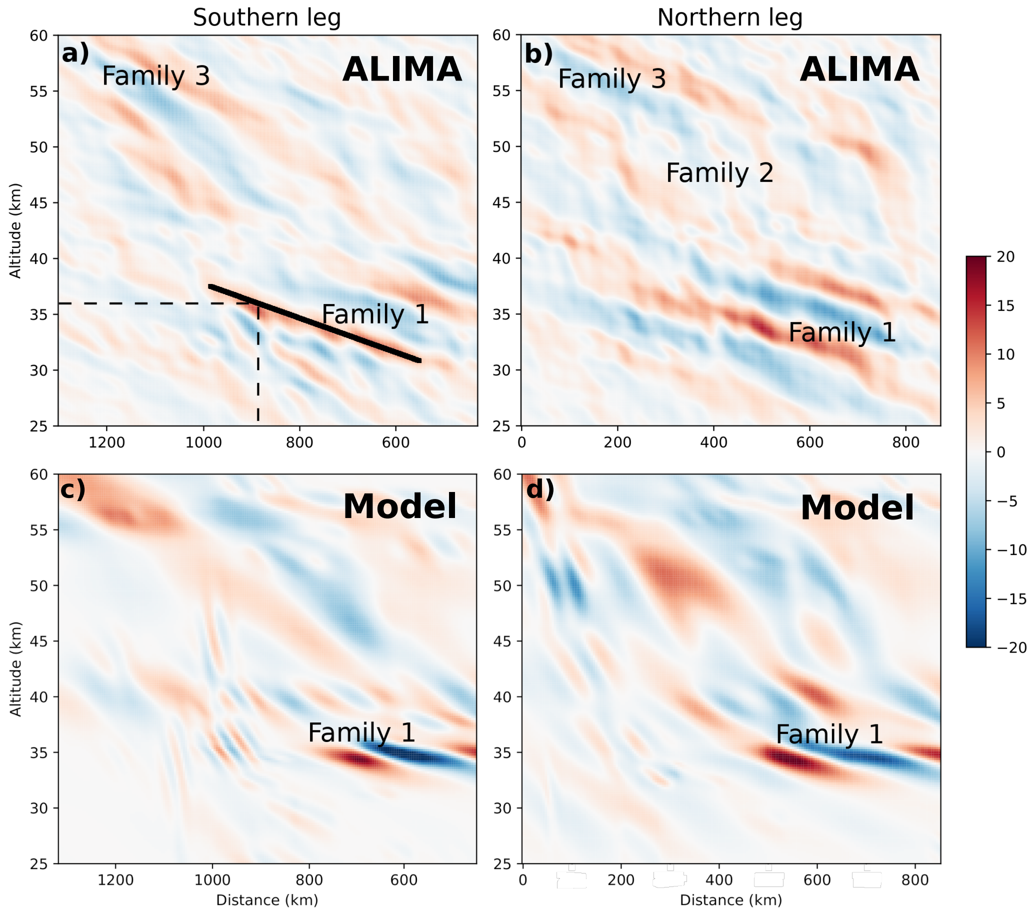

Figure 7. ALIMA temperature perturbations (in K) of the southern (a) and northern (b) leg. This is compared to the temperature perturbation from the mountain wave model of the same legs (c – southern leg and d – northern leg). Plots c and d are valid for 05:00. The x-axis is distance from the start of the respective flight leg. The eastern part of the southern leg is not shown here in order to have the same distance scale as the northern leg. Plots a and b show westward tilted GW phase fronts only (i.e. upward and westward propagating GWs, see Sect. 2.1.2). Note the three distinctly different wave packets, here named family 1, 2, and 3. Plots c and d do not see the same GWs for family 2 and 3 (see text for details). The solid and dashed lines indicate the method of determining phase orientation on horizontal plots, see text for details.

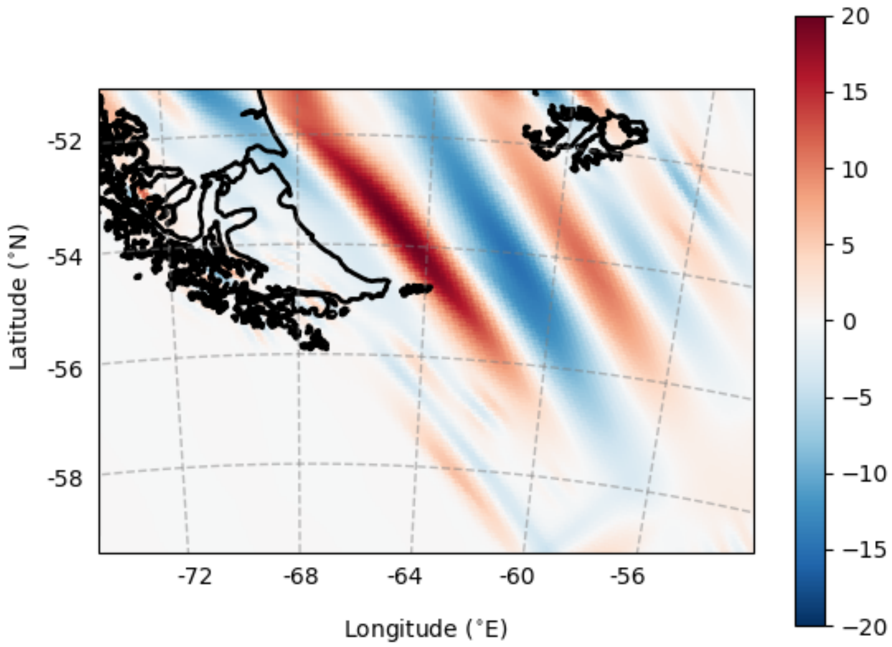

Figure 8. A horizontal cut at 34 km through temperature perturbation (in K) from family 1 as represented by the mountain wave model. Note how far the mountain waves propagate westwards and southwards into the Drake Passage. From this it is clear that GWs from topographic origin do propagate southwards into the Drake passage.

3.3.1 ALIMA: GW Family 1

Family 1 is clearly distinguished between 32 km to 40 km on both legs (Fig. 7a and b). From a single curtain we can obtain a vertical wavelength, but not an accurate horizontal wavelength and no orientation. Combining the vertical curtain with the horizontal cuts (e.g. Fig. 9) forms a 3-D picture where these can be determined. Phase fronts were approximated linearly in the vertical cut by drawing lines along the phase fronts (e.g. between 32 km and 38 km to identify the GWs — solid black line in Fig. 7a). Where the fitted line crossed a respective altitude the longitude was noted (dashed line Fig. 7a) and marked on the corresponding leg in the horizontal plot (Fig. 9). The phase orientation was obtained by connecting these longitudes, forming the phase fronts in Figures 9 and 10. By using this method we have a more complete picture. The racetrack flight pattern hence allows the determination of an accurate horizontal wavelength and orientation from ALIMA data exclusively.

Figure 9 is dominated by a long horizontal wavelength GW. For illustration one cold and warm phase front of the GW packet is drawn in. The blue and red phase fronts of both legs show a wavevector that points to the south-west (250° — measured on the drawn phase fronts). The horizontal wavelength is determined to be 473 km. Using ALIMA data that did not undergo the wavelet transform the amplitude is determined as 15 K. Horizontal cuts at multiple altitudes (seconded by the vertical cuts) show a vertical wavelength of 7.7 km. The ground-based phase speed is calculated using the dispersion relation (Eq. 1) and reveal a nearly stationary GW, which is common for mountain waves. This means that we can safely assume the GW remained stationary in time and space in the horizontal over the two legs for family 1.

Geldenhuys et al. (2021) state that whenever possible two or more pieces of evidence are required to diagnose a source. The first piece of evidence is the mountain wave model showing approximately the same GW as in the observations, implying its a mountain wave. To confirm this the 3-D wavevector of family 1 was backtraced with GROGRAT to the Andes. The ray traced from 36 km to directly above the Andes main ridge at ≈52°S. Combining the results from the mountain wave model and GROGRAT we have confidence the source of family 1 is indeed the Andes main ridge.

3.3.2 ALIMA: GW Family 3

Family 3 exists between 51 km and 60 km on Figure 7a and b. Figure 10 shows a clear westward slant of phase fronts with altitude between 53 km and 55.5 km. Figures 7 and 10 indicate a GW with a vertical wavelength of 7.5 km. Raw temperature residual data (before applying the 2-D Morlet continuous wavelet transform) show an amplitude of 7 K. The dashed phase fronts suggest an initial orientation of 282° and a horizontal wavelength of 291 km.

The dashed phase fronts on Figure 10 form a curious Y-shape pattern with phase lines from the three fronts meeting around 58°S. The most likely explanation is that the GW is not stationary and the phase propagation is to the east. This would stretch the wavelength on the northern leg and shorten it on the southern leg similar to a Doppler shift effect between phase velocity and aircraft movement. The GW has a non-zero ground-based phase speed. To correct for the non-stationarity we follow an iterative approach of determining the wavelength and phase speed, correcting for the phase speed and determining a new wavelength. We explain this for 53 km as an example on Fig. 10 top. Combining the fact that this is an upward propagating GW (see Sect. 2.1.2) and the westward phase slant with height (Figs. 7a, b, and 10) as well as the wind direction we know the GW wave vector points in an approximate westwards direction. To calculate the ground-based phase speed in the x-direction we need zonal wavenumber k (-1.87e-5 m^{-1} is the average between the two legs), meridional zonal number l (0 m^{-1}), vertical wavenumber m (8.3e-4 m^{-1}), stability (N^2 =2.276e-4 s^{-2}), scale height (7683 m), and zonal wind

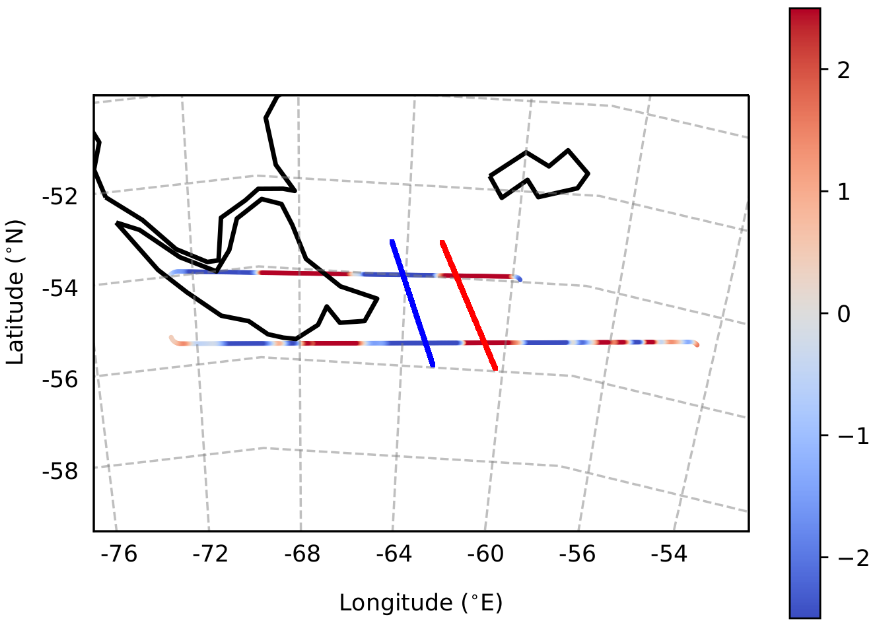

Figure 9. Temperature perturbation (in K) component showing the upward propagating GW as observed by ALIMA at 36 km. In an attempt to mask out short wavelength GWs, a colour scale is chosen where the temperature amplitude saturates at 2.5 K. Combining the northern and the southern legs and focusing on the long horizontal wavelength GWs, we can now form a 3-D picture. The drawn in phase fronts were determined with the help of vertical cuts. For the first time ALIMA data are used exclusively to determine GW phase orientation. From west to east we see two full wavelengths starting with a cold phase front.

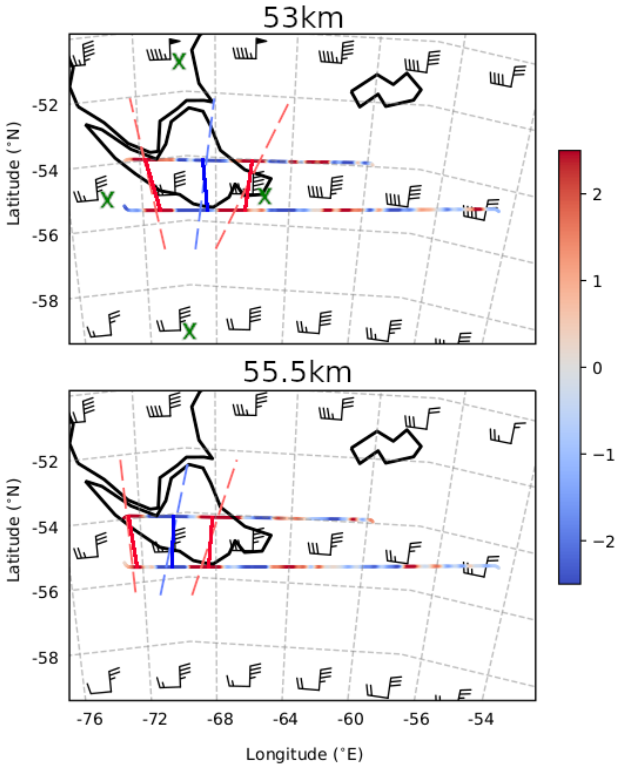

Figure 10. ALIMA temperature residuals (in K) showing upward propagating GWs at 53 km and 55.5 km. The background ERA5 zonal and meridional winds are shown in wind barbs. The barbs are similar to Fig. 1. Note the winds have a decreasing trend from northwest to southeast and with increasing altitude. The zonal wind speed is also generally weaker than the meridional wind speed. The dashed lines represent the phase fronts as determined from the vertical cut (Sect 3.3.1). The dashed phase fronts are then corrected (solid lines connecting the two race-tracks) to compensate for GW propagation (See Eq. 6 and corresponding text). The green X's on the top plot are used to predict the refraction in Sect. 4.

(v =30 ms^{-1}) obtained from ALIMA observations and ERA5. The calculated intrinsic phase speed in the x-direction is -16.96 ms^{-1}. The zonal wind speed is stronger than the intrinsic phase speed and the GW packet drifts eastwards at 13 ms^{-1} (and 13.1 ms^{-1} at 55.5 km). This means that when observing the warm phase front in the southern leg, the same phase front was located further westward than what it was observed in the northern leg in Figure 10. The phase correction is calculated by:

$$\text{correction} = (\text{reference time} - \text{observed time}) \cdot \text{ground-based phase speed} \tag{6}$$

with a reference time of 05:30. The solid lines between the flight tracks show the corrected phase lines. This correction reduces the Y-shape of the phase fronts and provides a more natural looking GW packet.

The new cold phase fronts (solid blue lines) suggest orientations of 262.8° at 53 km and 270.4° at 55.5 km. Raytracing this new and more accurate 3-D wavevector in GROGRAT shows the origin of this GW lies upwind of the Andes (Fig. 11); another indication of a non-orographic source (the non-stationary GW phase speed being the first). Some weak evidence of a jet generated GW exist, however, conclusive evidence is missing. A peak in WKB values from 0.1 to 0.45 exist at 24 km — a value of 0.45 is not considered a WKB violation but its worth noting the peak. No increased values of the cross-stream Lagrangian Rossby number was found in the region. However, an increase in the cross-stream ageostrophic wind was detected at 24.4 km (refer to (Zülicke & Peters, 2006; Geldenhuys et al., 2021) for the calculation of these parameters). On Figure 11b the ERA5 data confirms the upwind GW. The GW signal is weak near the WKB peak. Also, between -2000 to -2200 km and directly above the ray path a weak fishbone (or V-shaped) structure is identified. That makes three weak signals that indicates a jet generated GW. Using a rotary analysis technique, de la Torre et al. (2022) found predominantly downwards propagating GWs upwind of the Andes below 25 km — this would be in agreement with an out of balance jet at ≈24 km. This provides a curious case where a GW propagated for ≈1500 km just to be observed over a mountain. This highlights the fact that a source can not simply be determined by pure co-location as already mentioned in Krisch et al. (2020); Geldenhuys et al. (2021); Strube et al. (2021).

Evidence also exists for a mountain wave present in this region (Fig. 7c and d). The mountain wave and the non-orographic GW have very different characteristics suggesting that this is not the same GW packet. This altitude layer is a sensitive region with high gradients where the outcome depends highly on the details of the model atmospheric background and the details of the model. There is also evidence that in this region different sources coalesce. Given that above 40 km the reliability of model data is known to decrease (see Sakazaki et al. (2018); Ern et al. (2021)), we have insufficient information to disentangle this completely.

4 Refraction: Causality and Consequence

4.1 How do GWs refract?

This section will briefly explain how the GWs refract using the case of family 3. This section does not intend to provide an exact solution of refraction, but rather to describe its general behaviour. Horizontal wavelength and wave direction (which depends on the wavelength in the x- and y-direction) of a GW change in the presence of a horizontal wind gradient (e.g. Ehard et al., 2017). This is described by Equations 2 and 3 from Lighthill (1978) (also in Marks and Eckermann (1995)). In the presence of strong horizontal wind gradients the first two terms in Equations 2 and 3 are the dominant ones. We therefore neglect the smaller terms to obtain:

$$\frac{dk}{dt} = -k\frac{\partial u}{\partial x} - l\frac{\partial v}{\partial x} \tag{7}$$

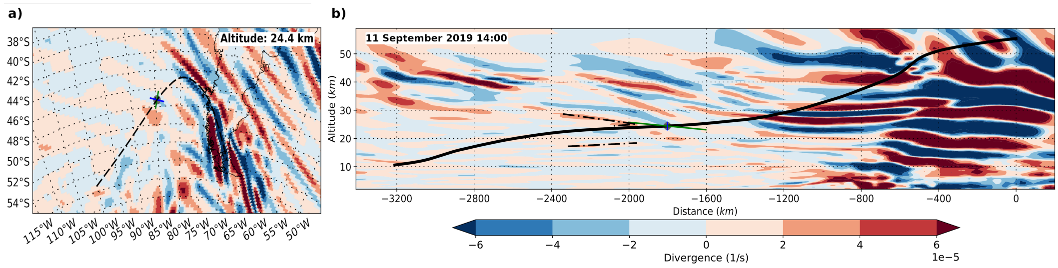

Figure 11. Divergence of ERA5 horizontal winds along the GROGRAT raytrace started at 55.5 km. Both plots are valid for 11 September at 14:00. Panel a shows the horizontal cut at 24.4 km. Panel b shows a vertical cut along the raypath. The dash dot lines show the different phase slants and guide the eye to the weak V-shape pattern (see text for details). The black, blue and green line is similar to Fig. 5.

$$\frac{dl}{dt} = -k\frac{\partial u}{\partial y} - l\frac{\partial v}{\partial y} \tag{8}$$

Family 3 experiences a significant amount of shear on the edge of the polar vortex and serves as a good example to understand refraction from both theory and observation. Refraction is evident in the solid phase lines between 53 km and 55.5 km on Figure 10. The wind barbs on the plot represent ERA5 background zonal and meridional winds without the GW perturbation. The centre of the displaced and elongated vortex is located to the south (Fig. 2) and results in a decreasing wind speed from north-west to south-east (Fig. 10). This horizontal shear creates favourable conditions for refraction. Using the winds as input into Equations 7 and 8 we can predict the refraction in time.

The wind gradient is determined in the x- and y-direction between the green X's on Figure 10. The gradients in the x-direction are negative (Table 1) while being positive in the y-direction. Under normal non-displaced vortex conditions one would expect no gradient in the x-direction and a positive gradient in the y-direction. By placing these gradients together with the wavenumber k (calculated from new solid phase lines -1.93e-5 m^{-1}) and l (-2.44e-6 m^{-1}) into Equations 7 and 8 we can approximate the derivative ${}^{dk}/_{dt}$ and ${}^{dl}/_{dt}$ as ${}^{\Delta k}/_{\Delta t}$ and ${}^{\Delta l}/_{\Delta t}$ (documented in Tab. 2). Under the assumption that we see the same GW packet, Δt can be estimated from the time it takes the GW to propagate from 53 km to 55.5 km; which is 1 hr[4]. According to the resultant Δk and Δl, the total horizontal GW wavelength from 53 km to 55.5 km will reduce from 323 km to 303 km. The predicted change in angle of orientation is from 262.8° at 53 km to 269.1° at 55.5 km. This compares remarkably well with the 270.4° we observe on Fig. 10 and the related discussion in Sec. 3.3.2. The GW is expected to refract by another 5° from 55.5 km to 60 km. After the phase correction applied in the previous section (see Fig. 10), the ALIMA observations can serve as an example for refraction.

From this section it is evident that refraction greatly depends on the wavelength and the wind gradient. The wind shear experienced during this flight was anomalously strong for this time of the year. This was caused by the displaced vortex and sudden stratospheric warming (Sect. 3.1), which created a situation better than most to study refraction.

[4] The vertical phase speed varies between 0.5 ms^{-1} (1.8 kmh^{-1}) to 0.75 ms^{-1} (2.7 kmh^{-1}) for this GW. For convenience we assume it at 2.5 kmh^{-1}.

Table 1. Parameters for input into Equations 7 and 8 determined from Figure 10. The distances in ∂x and ∂y are 535.1 km and 889.6 km respectively.

Altitude	∂u in x	∂v in x	∂u in y	∂v in y
53 km	-10 ms^{-1}	-10 ms^{-1}	25 ms^{-1}	15 ms^{-1}
55.5 km	-5 ms^{-1}	-5 ms^{-1}	25 ms^{-1}	5 ms^{-1}

Table 2. Calculated values to predict the new orientation using Equations 7 and 8 with values stated in Table 1. Wavenumbers k and l are -1.93e-5 m^{-1} and -2.44e-6 m^{-1} at 53 km.

Altitude	$\frac{\Delta k}{\Delta t}$	$\frac{\Delta l}{\Delta t}$	Δk	Δl	Predicted Orientation
53 km	-4.06e-7 $\mathrm{m}^{-1}\mathrm{s}^{-1}$	5.84e-7 $\mathrm{m}^{-1}\mathrm{s}^{-1}$	-1.46e-6 m^{-1}	2.1e-6 m^{-1}	269.1°
55.5 km	-2.03e-7 $\mathrm{m}^{-1}\mathrm{s}^{-1}$	5.56e-7 $\mathrm{m}^{-1}\mathrm{s}^{-1}$	-7.31e-7 m^{-1}	2.0e-6 m^{-1}	274.4°

4.2 What is the impact of the refracting GWs?

In this section we discuss how refraction impacts the atmosphere through taking up additional GWMF and by modifying the propagation path of the GW. Five GROGRAT experiments are conducted to illustrate this. All five experiments use the GW characteristics at the source of the GLORIA observed GW (obtained by backtracing — Sect. 3.2.3). The forward raytracing experiment starts directly above the source at 4 km.

The first experiment (ray #0) is the control experiment and is used to compare to different scenarios. Ray #0 represents the most up to date physics and should be the closest to reality. This entails the use of 4-D propagation setup and a high-resolution background as described in Section 2.3. The GW represented by ray #0 in Figure 12 rapidly propagates into the stratosphere in a south-eastward direction. Ray #1 uses the same setup but with an enhanced wind gradient in a stronger background flow. The enhanced gradient was obtained by multiplying the background wind with a factor of 1.5. Ray #2 represent the 1-D column parameterisation scheme employed by models. This ray can only propagate in the vertical and can not undergo refraction. Ray #3 is used to reproduce the experiment of Hasha et al. (2008). Hasha et al. (2008) used 3-D raytracing with low-resolution model background data. Input of GW characteristics were determined by a model parameterisation scheme. They found that there is no noteworthy reason to include refraction and horizontal propagation of mid-frequency GWs into models.

Richard Feynman said that proper experiment design requires you to first reproduce the results from previous work before you can build on that (Leighton & Feynman, 1985). With this in mind the experiment of Hasha et al. (2008) was reproduced as closely as possible, but keeping it comparable to the results in this study. To keep the results comparable, the same (as ray #0 to #2) background conditions and ray initial conditions were used (which is a mid-frequency GW). Only the GROGRAT setup was changed to represent the 2008 experiment. Ray #3 on Figure 12 was raytraced with the 3-D propagation setup (Sect. 2.3) in a coarse resolution background. Analogous to the Hasha et al. (2008) experiment the background consisted of a vertical (horizontal) resolution of 1.3 km (2.5°). The resulting forward raytrace of ray #3 follows the same horizontal trajectory as ray #0 at first but diverges towards the end of the ray. Ray #3 remains in the troposphere and at a much lower latitude than ray #0 (which ends at 75°S). Compared to the control ray (ray #0), the relative error in ray #3 is 10° of latitude and 35 km in altitude. The incorrect location of GWMF deposition by ray #3 will result in a noteworthy difference compared to ray #0. More importantly, the results from Hasha et al. (2008) are not reproduced as the GWMF deposit takes place at a significantly lower lat-

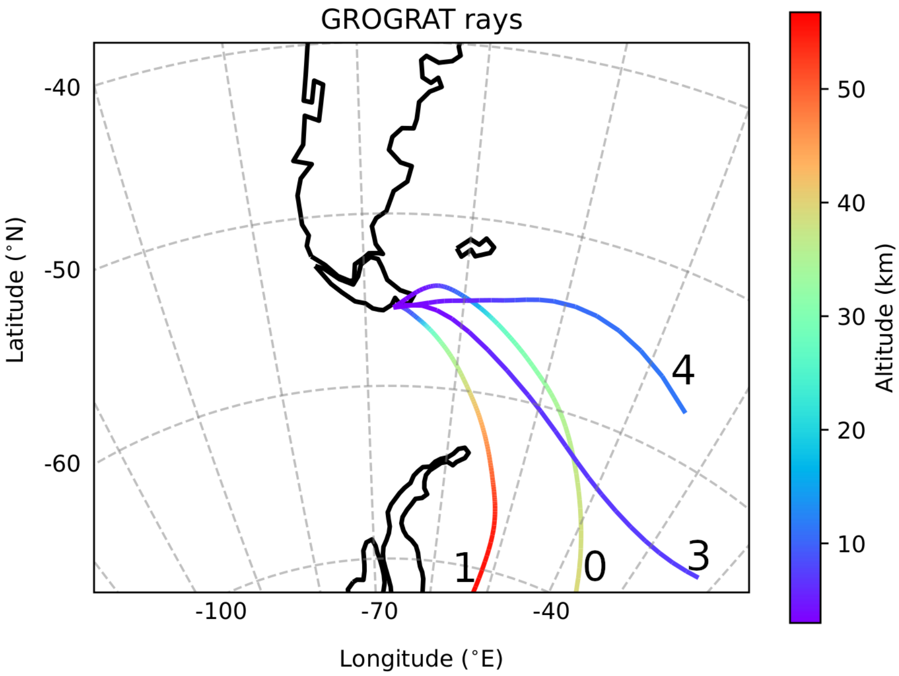

Figure 12. GROGRAT experiments during forward tracing of the GLORIA observed GW. Ray #0 shows raytracing using the 'normal' setup with 4-D propagation in a high-resolution background. Ray #1 uses the same 4-D propagation setup but uses a background u and v wind, which was multiplied by a factor of 1.5. Ray #2 is not depicted here as it will only show as a dot above the starting location. Ray #3 attempts to reproduce the results of (Hasha et al., 2008) and uses a coarse resolution background and only 3-D propagation setup. Ray #4 use the exact same settings as ray #3 but use background conditions of the 'normal' year 2018.

itude. With the anomalously different wind regime of 2019, we can not come to the same conclusion as Hasha et al. (2008).

In another attempt to reproduce the results of Hasha et al. (2008) we used background conditions of a 'normal' year. In a new experiment, represented by ray #4 on Figure 12, we use the exact same propagation setup and resolution but using the non-stratospheric-warming year of 2018 as background input into GROGRAT. On 4 September 2018 at 06:00 a similar (to 11 September 2019) tropospheric synoptic system existed where a cold front brushed over the southern Andes with a ridging high pressure system behind that. We assume that this synoptic system will result in similar GWs to the GLORIA observed GWs. Raytracing the GW in the 2018 conditions we find after 25 h of propagation the ray (again) remains in the troposphere, but only deviates by 2° of latitude from its source latitude. The small difference in latitude reflects a similar result to the conclusion of Hasha et al. (2008). Ignoring the incorrect altitude of the ray, we can say that the GW will produce drag at roughly the correct latitude. This experiment correctly reproduces the result of Hasha et al. (2008); horizontal propagation and refraction can be ignored without serious repercussions. However, in different circumstances (like this case of 2019 with a weak and displaced vortex) this does not apply. The two experiments used to reproduce Hasha et al. (2008) confirms the finding of Durran (2009) who stated that the impact of refraction on GWMF is case dependent. Chen et al. (2005) and Durran (2009) found in their idealised numerical study that the GWMF is enhanced in regions of divergence and reduced in regions of convergence.

Ray #2 was restricted to vertical propagation and is not identifiable on Figure 12 (as it is only a dot at the starting location below ray #3). Ray #2 attained a maximum altitude of 42 km (similar to our normal conditions represented by ray #0). The drag deposited from ray #2 will be at the correct altitude, but the incorrect latitude; a major shortcoming (similar to ray #3).

Ray #1 uses background conditions with a stronger wind and an increased wind gradient. By multiplying the background wind with a factor of 1.5 we obtain a total wind speed more representative to normal (compared to the year 2020) stratospheric polar vortex wind speeds. The multiplication also results in a larger wind gradient. It is known that GWs prefer stronger winds to propagate in (if the wind is not too strong to create a propagation lid). Thus, it is no surprise to see ray #1 reach the highest altitude at 57 km. Ray #1 propagates further south and reaches polar vortex altitudes sooner compared to ray #0. The stronger wind with increased gradient creates an even more perfect setting (compared to ray #0) for GW propagation and refraction.

The GWMF of the 4 rays are compared in Figure 13. Ray #1 dominates the graph and clearly the stronger wind results in a higher GWMF. GROGRAT takes k, l and ground-based frequency as input and calculates the vertical wavelength from intrinsic phase speed. The intrinsic phase speed is affected by the higher background wind speed, which results in a larger vertical wavelength. This results in an artificial higher GWMF value at the start of the ray. Ray #0, #1 and #2 agree somewhat with regards to the altitude where most of the drag is deposited. Ray #3 compares the worst as the ray never reaches the stratosphere. The comparison of the GWMF makes it clear that not only the deposition location differs (as described in the first part of this subsection), but also the amount of GWMF. Most of the community (and in fact all GW parameterisations) only consider GWMF decreasing with altitude. Ray #2 and #3 follow this assumption, but ray #0 and #1 do not. To investigate this increase in GWMF we consider only ray #0 in Figure 14.

The GWMF of ray #0 in Figure 14 show a clear increase between 4 km and 30 km. A strong decrease of horizontal wavelength corresponds with these altitudes. In Section 3 we established that refraction is directly linked to the wavelength of the GW (and in turn the wavelength is linked to the wind gradient). Figure 14 confirms the link between GWMF

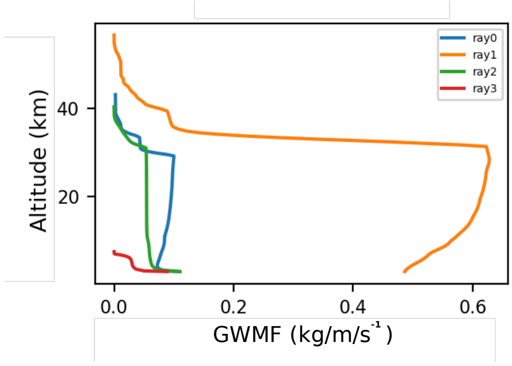

Figure 13. The GWMF along rays #0 to #3. Note the increase in the GWMF along ray #0 and #1, as opposed to ray #2 and #3, which only decrease with altitude.

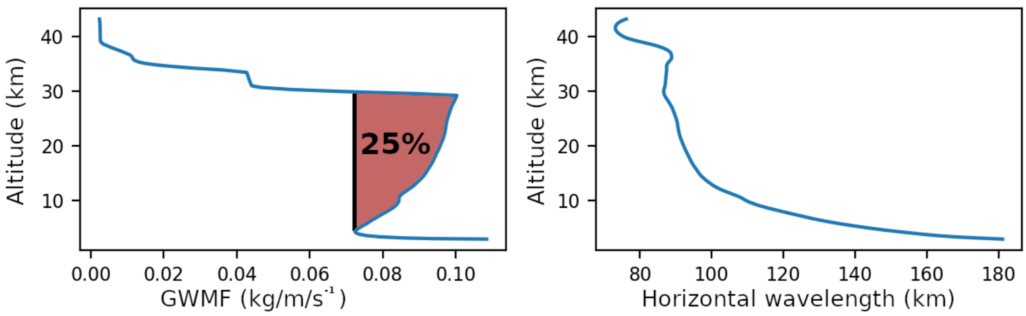

Figure 14. The GWMF and horizontal wavelength along ray #0. Note the maximum change in horizontal wavelength corresponds to the GWMF increase between 4 km and 30 km. An increase of 25.7% is observed.

and horizontal wavelength and therefore suggest a link to refraction. To understand this we look at the GWMF equation for a single wave (absolute momentum flux Equation 1 from Ern et al. (2015)):

$$\mathrm{GWMF} = \frac{1}{2}\rho_0 \frac{\lambda_z}{\lambda_h}\left(\frac{g}{N}\right)^2 \left(\frac{\hat{T}}{T}\right)^2 \tag{9}$$

where λ_z is vertical wavelength and λ_h is horizontal wavelength. The GWMF equation depends on the horizontal wavelength in the denominator. This means that if the horizontal wavelength decreases (Fig. 14 right) the GWMF increases (Fig. 14 left). Similarly, in an idealised numerical study Chen et al. (2005) found that the GW wavelength decrease if it propagates through wind divergent regions, increasing the GWMF of the GW. This finding remained valid looking at a single wave and at the total GW packet.

The change in wavelength (hence refraction) makes a significant contribution to the total GWMF of the GW packet. The GWMF along ray #0 increase by as much as 25.7% (scaled by the amount at forcing altitude). Accordingly, ray #0 can deposit a 1/4 more momentum and have a stronger effect on the background flow. The GWMF of ray #1 increases by 30% along the ray. This shows that a stronger wind with a larger wind gradient will increase the amount of missing drag in the model. In a numerical study (on the same date), (Alexander et al., 2022) found a general increase in average GWMF with altitude calculated zonally in the rectangle defined by 45°S 63°W and 60°S 77°W. Similar to Figure 14, they found a general increase with a peak in the GWMF at ≈30km. This can be an indication that all the GWs in this region refract similarly with an increase in GWMF.

It is possible that the increase in GWMF averages out in time with all the other cases where GWMF decreases as a result of refraction (Durran, 2009). This can mean that this process does not have a meaningful impact over a longer time scale, however, this still needs to be confirmed. Even if the GWMF does average out over a time period, it can still have an impact on local dynamics. Literature state that short but sustained bursts of GW activity can have marked impact on dynamics — for example Samtleben et al. (2020) found it can help to generate a sudden stratospheric warming. This would mean a few days with an increased amount of GWMF can have an important impact.

The five experiments (four rays plus the repeated Hasha-experiment) discussed in this section bring the importance of refraction (and horizontal propagation) forward. Not only do these processes affect where the GWMF is deposited, they also affect the amount of GWMF deposition.

5 Summary

This article provides the first detailed and compelling analysis of gravity wave (GW) refraction using high-resolution observations during a sudden stratospheric warming. The reader is to keep in mind that the sudden stratospheric warming resulted in winds that are not representative of the normal this time of year. This article builds on previous studies like Ehard et al. (2017) by providing high-resolution observations of the process of refraction, explaining this with the equations available in literature and by showing through raytracing experiments the impacts of refraction on GWMF (GW momentum flux). Observations were obtained on 12 September 2019 during the SouthTRAC campaign with the airborne GLORIA infrared limb imager and the ALIMA Rayleigh lidar. GLORIA observes the GWs below and ALIMA above flight altitude. The GLORIA retrieval used the CO_2 lines (936.8 – 938.6, 939.2 – 941.0 and 942.2 – 944 cm^{-1}) to create a 1-D retrieval and a 3-D dataset. The observed GW characteristics combined with the GROGRAT (Gravity-wave Regional Or Global Ray Tracer) raytracer reveal the source of the GW observed by GLORIA is the mountains on the south coast of Patagonia. Tracing the GWs forward produce an excellent match between the GROGRAT reconstructed GWs, high-resolution WRF (3 km in the horizontal and 0.5 km in the vertical — Weather Research and Forecasting model) data and the ALIMA observed GWs. This acts as direct and high-resolution verification of GROGRAT versus observation and model. GLORIA 1-D data shows refraction of 16° between 8 km and 12 km. The GLORIA 1-D orientation at 8 km is also validated with satellite data, which shows an orientation of ≈240° between ≈4 km and ≈8 km.

ALIMA curtains reveal three distinctly different GW families (Fig. 7a and b). The curtain retrievals of ALIMA form a 2-D dataset, but through creative flight planning (flight track/experimental design) a 3-D dataset is obtained. By flying a racetrack (containing two parallel legs) the data from both legs are combined. For the first time this allowed an accurate horizontal wavelength and orientation observation from lidar measurements — allowing a high-resolution refraction study. However, this is only valid if the GW remains stationary across the two legs. The dispersion relation combined with the 3-D wavevector show that family 1 is stationary in the horizontal and family 3 is drifting downstream (eastwards) with time. The second GW family is observed in one curtain only and thus no 3-D wavevector can be determined. To determine an accurate orientation of family 3 the phase fronts are corrected for horizontal propagation (Fig. 10). The newly available 3-D wavevector of two of the three wave families are used in GROGRAT to raytrace the GWs. Family 1 traces backwards to the main Andes ridge at 52°S. Family 3 traces backwards upstream of South America and has a non-orographic source. A mountain wave model indeed reproduced family 1 of the three GW families and two GW critical layers (Fig. 7c and d). The model proved to be a great tool to pin point the location of topographical sources. The model only considers mountain waves and thus proposes the source of family 1 is orography. The mountain wave model also illustrated that mountain waves can propagate a substantial distance from their source and into the Drake passage. This highlights the fact that mountain waves contribute to the 60°S problem.

Family 3 and ERA5 background winds provide the opportunity to explain refraction in detail (Fig. 10). Refraction simply put is the wavelength in x- and y-direction changing. Through the use of Eqs. 7 and 8 it is shown that refraction depends on a change in wavelength, while the change in wavelength depends on the wind gradient. As an illustration, refraction is correctly predicted from 261° at 53 km to 270° at 55.5 km. The prediction is solely made by using the above mentioned equations, observed wavelengths, background winds and the calculated vertical propagation speed (to account for time). It is shown that refraction heavily relies on a background wind gradient.

Refraction makes an important contribution to the amount and the distribution of GWMF. A GW packet propagates roughly along its phase lines, which makes the orientation very important to horizontal propagation. Five GROGRAT experiments are used to illustrate the importance of refraction. The experiments use forward raytracing from directly above the source of the GLORIA observed GW. Figure 12 shows the impact on the location of GWMF deposition based on including or excluding refraction and horizontal propagation. The first experiment (also the control experiment — ray #0) represents the most up to date physics and highest resolution background. Ray #1 shows that a stronger wind with a stronger wind gradient allows the ray to reach higher altitudes, propagate further south and refract more. Ray #2 represents the current 1-D parameterisation schemes employed by models. This ray can only propagate in the vertical with no refraction. This ray reproduces GWMF deposition at the correct altitude but with the source latitude being incorrect with an error of 20°. Ray #3 is an attempt at reproducing the results of Hasha et al. (2008) who stated that refraction and horizontal propagation can be neglected in models.

Similar to Hasha et al. (2008) ray #3 uses a low resolution and only 3-D propagation setup (the background atmosphere remains constant with time). The results from this ray show that 4-D propagation and a high-resolution background is important when raytracing (Fig. 12). Ray #3 propagates in a south-eastward direction and remains in the troposphere (very different from ray #2). The deposition latitude in ray #3 is vastly different from the source latitude. This shows that using the anomalously different sudden stratospheric warming background winds we can not come to the same conclusion as Hasha et al. (2008). In another attempt to reproduce their experiment the same ray #3 is raytraced in the background winds of 4 September 2018 (forming ray #4). This date represents a 'normal' year with tropospheric conditions similar to the flight date of 12 September 2019. The ray in the 2018 background remains in the troposphere and only deviates by 2° of latitude. We conclude that we can successfully reproduce the result of Hasha et al. (2008) and that their conclusion holds in this instance under strong polar vortex conditions. Weak vortex conditions (when the vortex is usually stretched or displaced) produce strong wind shear, which allows for more refraction and further meridional propagation. This confirms the finding by Durran (2009) who stated the effect of refraction on the GWMF differs from case to case. A shortcoming of this study is that it only uses two (if you count the 2018 raytrace) case studies, ideally this needs to be checked over a longer timeframe and is part of an ongoing study.

The real impact of refraction is revealed by the GWMF along the rays. Figures 13 and 14 show an increase in GWMF along the ray path. The information along ray #0 show that the strongest increase in GWMF coincides with the strongest decrease in horizontal wavelength. The GWMF equation (Eq. 9) confirms a link with the horizontal wavelength in the denominator. Ray #0 (#1) reveal a 25.7% (30%) increase in the GWMF along the ray. This is a significant increase and implicates that some non-resolved GWs in the model have a quarter too little GWMF during weak vortex conditions. This can make a sizeable contribution to the missing drag identified by McLandress et al. (2012) and Garcia et al. (2017). McLandress et al. (2012) state that "modelers should give serious thought" to account for meridional propagation of GWs in parameterisation schemes. This article shows that it is empirical that model parameterisation schemes should not only include horizontal propagation, but also refraction physics to improve representation of atmospheric dynamics.

Open Research

Acknowledgments

The authors gratefully acknowledge the computing time granted by the JARA Vergabegremium and provided on the JARA Partition part of the supercomputer JURECA (Jülich Supercomputing Centre, 2018) at Forschungszentrum Jülich. We would like to acknowledge everyone that contributed to the campaign, especially the FX team and the pilots. PA was funded by grant ANPCYT PICT 2018-653. The computational resources used for WRF were provided by the HPC center DIRAC, funded by Instituto de Física de Buenos Aires (UBA-CONICET) and by SNCAD MinCyT initiative.

References

Alexander, M. J., Geller, M., McLandress, C., Polavarapu, S., Preusse, P., Sassi, F., ... Watanabe, S. (2010). Recent developments in gravity-wave effects in climate models and the global distribution of gravity-wave momentum flux from observations and models. *Quart. J. Roy. Meteorol. Soc.*, *136*, 1103-1124. doi: 10.1002/qj.637

Alexander, P., de la Torre, A., Llamedo, P., Hierro, R., Marcos, T., Kaifler, B., ... Hormaechea, J. L. (2022). The coexistence of gravity waves from diverse sources during a southtrac flight with optimal vertical propagation conditions. *J. Geophys. Res.*. (to be submitted)

Amante, C., & Eakins, B. (2009). *Etopo1 1 arc-minute global relief model: Procedures, data sources and analysis.* National Centers for Environmental Information, NESDIS, NOAA, U.S. Department of Commerce. (last access: 20 February 2020) doi: 10.7289/V5C8276M

Bacmeister, J., Newman, P., Gary, B., & Chan, K. (1994, JUN). An algorithm for forecasting mountain wave-related turbulence in the stratosphere. *Wea. Forecast.*, *9*(2), 241-253. doi: 10.1175/1520-0434(1994)009⟨0241:AAFFMW⟩2.0.CO;2

Boeloeni, G., Kim, Y.-H., Borchert, S., & Achatz, U. (2021). Toward Transient Subgrid-Scale Gravity Wave Representation in Atmospheric Models. Part I: Propagation Model Including Nondissipative Wave–Mean-Flow Interactions. *J. Atmos. Sci.*, *78*, 1317-1338. doi: 10.1175/JAS-D-20-0065.1

Chen, C., & Chu, X. (2017). Two-dimensional morlet wavelet transform and its application to wave recognition methodology of automatically extracting two-dimensional wave packets from lidar observations in antarctica. *J. Atm. Sol.-Terr. Phys.*, *162*, 12,737–12,750. doi: 10.1016/j.jastp.2016.10.016

Chen, C., Durran, D., & Hakim, G. (2005). Mountain-wave momentum flux in an evolving synoptic-scale flow. *J. Atmos. Sci.*, *62*(9), 3213 - 3231. doi: 10.1175/JAS3543.1

de la Torre, A., Alexander, P., Llamedo, P., Hierro, R., Marcos, T., Kaifler, B., … Hormaechea, J. L. (2022). A spectral rotary analysis of gravity waves: An application to a southtrac flight. *J. Geophys. Res.*. (to be submitted)

de la Camara, A., Lott, F., & Hertzog, A. (2014, NOV 16). Intermittency in a stochastic parameterization of nonorographic gravity waves. *J. Geophys. Res. Atmos.*, *119*(21), 11905-11919. doi: 10.1002/2014JD022002

de la Camara, A., Lott, F., Jewtoukoff, V., Plougonven, R., & Hertzog, A. (2016, AUG). On the gravity wave forcing during the southern stratospheric final warming in LMDZ. *J. Atmos. Sci.*, *73*(8), 3213-3226. doi: 10.1175/JAS-D-15-0377.1

Doernbrack, A., Eckermann, S. D., Williams, B. P., & Haggerty, J. A. (2021). Stratospheric gravity waves excited by propagating Rossby wave trains. *J. Atmos. Sci.*. (under review) doi: 10.3390/atmos8030049

Dunkerton, T. J. (1984). Inertia gravity waves in the stratosphere. *J. Atmos. Sci.*, *41*, 3396-3404.

Durran, D. (2009). Comments on "gravity wave refraction by three-dimensionally varying winds and the global transport of angular momentum". *J. Atmos. Sci.*, *66*(7), 2150 - 2152. doi: 10.1175/2008JAS3013.1

Dörnbrack, A., Kaifler, B., Kaifler, N., Rapp, M., Wildmann, N., Garhammer, M., … Austin, E. J. (2020). Unusual appearance of mother-of-pearl clouds above el calafate, argentina (50°21's, 72°16'w). *Wea.*, *75*(12), 378-388. doi: 10.1002/wea.3863

Eckermann, S. D., & Marks, C. J. (1997). GROGRAT: a new model of the global propagation and dissipation of atmospheric gravity waves. *Adv. Space Res.*, *20*, 1253-1256.

Ehard, B., Kaifler, B., Dörnbrack, A., Preusse, P., Eckermann, S., Bramberger, M., … Rapp, M. (2017). Horizontal propagation of large amplitude mountain waves in the vicinity of the polar night jet. *J. Geophys. Res. Atmos.*, 1423-1436. Retrieved from `http://dx.doi.org/10.1002/2016JD025621` (2016JD025621) doi: 10.1002/2016JD025621

Ern, M., Diallo, M., Preusse, P., Mlynczak, M. G., Schwartz, M. J., Wu, Q., & Riese, M. (2021). The semiannual oscillation (SAO) in the tropical middle atmosphere and its gravity wave driving in reanalyses and satellite observations. *Atmos. Chem. Phys.*, *21*, 13763–13795. Retrieved from `https://acp.copernicus.org/preprints/acp-2021-190/` doi: 10.5194/acp-21-13763-2021

Ern, M., Hoffmann, L., & Preusse, P. (2017, JAN). Directional gravity wave momentum fluxes in the stratosphere derived from high-resolution AIRS temperature data. *Geophys. Res. Lett.*, *44*(1), 475-485. doi: 10.1002/2016GL072007

Ern, M., Preusse, P., & Riese, M. (2015). Driving of the SAO by gravity waves as observed from satellite. *Ann. Geophys.*, *33*(4), 483-504. doi: 10.5194/angeo-33-483-2015

Friedl-Vallon, F., Gulde, T., Hase, F., Kleinert, A., Kulessa, T., Maucher, G., … Ungermann, J. (2014). Instrument concept of the imaging Fourier transform spectrometer GLORIA. *Atmos. Meas. Tech.*, *7*(10), 3565-3577. doi: 10.5194/amt-7-3565-2014

Fritts, D., & Alexander, M. (2003, APR 16). Gravity wave dynamics and effects in the middle atmosphere. *Rev. Geophys.*, *41*(1). doi: 10.1029/2001RG000106

Fritts, D., & Rastogi, P. (1985). Convective and dynamical instabilities due to gravity wave motions in the lower and middle atmosphere: theory and observations. *Radio Sci.*, *20*, 1247-1277.

Garcia, R. R., Smith, A. K., Kinnison, D. E., de la Camara, A., & Murphy, D. J. (2017). Modification of the gravity wave parameterization in the whole atmosphere community climate model: Motivation and results. *J. Atmos. Sci.*, *74*(1), 275-291. doi: 10.1175/JAS-D-16-0104.1

Gelaro, R., McCarty, W., Suárez, M. J., Todling, R., Molod, A., Takacs, L., … Zhao, B. (2017). The modern-era retrospective analysis for research and applications, version 2 (MERRA-2). , *30*(14), 5419 - 5454. Retrieved from `https://journals.ametsoc.org/view/journals/clim/30/14/jcli-d-16-0758.1.xml` doi: 10.1175/JCLI-D-16-0758.1

Geldenhuys, M. (2022). On gravity wave parameterisation in vicinity of low-level blocking. *Atmospheric Science Letters*. (accepted)

Geldenhuys, M., Dyson, L., & van der Mescht, D. (2019). Blocking, gap flow and mountain wave interaction along the coastal escarpment of South Africa. *Theoretical and Applied Climatology*, *139*, 1291-1303. doi: 10.1007/s00704-019-03030-4

Geldenhuys, M., Preusse, P., Krisch, I., Zülicke, C., Ungermann, J., Ern, M., … Riese, M. (2021). Orographically induced spontaneous imbalance within the jet causing a large-scale gravity wave event. *Atmos. Chem. Phys.*. doi: 10.5194/acp-21-10393-2021

Geller, M. A., Alexander, M. J., Love, P. T., Bacmeister, J., Ern, M., Hertzog, A., … Zhou, T. (2013, SEP). A comparison between gravity wave momentum fluxes in observations and climate models. *J. Clim.*, *26*(17), 6383-6405. doi: 10.1175/JCLI-D-12-00545.1

Gupta, A., Birner, T., Dörnbrack, A., & Polichtchouk. (2021). Importance of gravity wave forcing for springtime southern polar vortex breakdown as revealed by ERA5. *Geophys. Res. Lett.*, *48*, e2021GL092762. doi: 10.1029/2021GL092762

Hasha, A., Bühler, O., & Scinocca, J. (2008). Gravity wave refraction by three-dimensionally varying winds and the global transport of angular momentum. *J. Atmos. Sci.*, *65*, 2892-2906.

Hauchecorne, A., & Chanin, M. L. (1980). Density and temperature profiles obtained by lidar between 35 and 70 km. *Geophys. Res. Lett.*, *7*, 565-568. doi: 10.1029/GL007i008p00565

Hersbach, H., Bell, B., Berrisford, P., Hirahara, S., Horanyi, A., Munoz-Sabater, J., … Thepaut, J.-N. (2020, JUL). The ERA5 global reanalysis. *Quart. J. Roy. Meteorol. Soc.*, *146*(730), 1999-2049. doi: {10.1002/qj.3803}

Hertzog, A., Souprayen, C., & Hauchecorne, A. (2001, SEP). Observation and backward trajectory of an inertio-gravity wave in the lower stratosphere. *Ann. Geophys.*, *19*(9), 1141-1155.

Hindley, N. P., Wright, C. J., Hoffmann, L., Moffat-Griffin, T., & Mitchell, N. J. (2020, NOV 28). An 18-year climatology of directional stratospheric gravity wave momentum flux from 3-D satellite observations. *Geophys. Res. Lett.*, *47*(22), e2020GL089557. doi: 10.1029/2020GL089557

Holton, J. R. (2004). *An introduction to dynamic meteorology.* Academic Press Limited. (3rd edition)

ICAO. (2005). *Manual on low-level wind shear.* International Civil Aviation Organization.

Jülich Supercomputing Centre. (2018). JURECA: Modular supercomputer at Jülich Supercomputing Centre. *Journal of large-scale research facilities*, *4*(A132). Retrieved from http://dx.doi.org/10.17815/jlsrf-4-121-1 doi: 10.17815/jlsrf-4-121-1

Kaifler, B., & Kaifler, N. (2021). A compact rayleigh autonomous lidar (CORAL) for the middle atmosphere. , *14*, 1715–1732. doi: 10.5194/amt-14-1715-2021

Kaifler, B., Kaifler, N., Dörnbrack, A., & Rapp, M. (2022). A case study of mountain wave momentum flux measurements in the middle atmosphere over the southern andes. *J. Geophys. Res.*. (to be submitted)

Kaifler, N., Kaifler, B., Ehard, B., Gisinger, S., Dornbrack, A., Rapp, M., … Liley, B. (2017, SEP). Observational indications of downward-propagating gravity waves in middle atmosphere lidar data. *J. Atm. Sol.-Terr. Phys.*, *162*(SI), 16-27. doi: 10.1016/j.jastp.2017.03.003

Kaufmann, M., Blank, J., Guggenmoser, T., Ungermann, J., Engel, A., Ern, M., … Riese, M. (2015). Retrieval of three-dimensional small-scale structures in upper-tropospheric/lower-stratospheric composition as measured by GLORIA. *Atmos. Meas. Tech.*, *8*(1), 81-95. Retrieved from http://www.atmos-meas-tech.net/8/81/2015/ doi: 10.5194/amt-8-81-2015

Kidston, J., Scaife, A. A., Hardiman, S. C., Mitchell, D. M., Butchart, N., Baldwin, M. P., & Gray, L. J. (2015). Stratospheric influence on tropospheric jet streams, storm tracks and surface weather. *Nature Geosci.*, *8*, 433-440. doi: 10.1038/ngeo2424

Kim, Y.-H., Boeloeni, G., Borchert, S., Chun, H., & Achatz, U. (2021). Toward Transient Subgrid-Scale Gravity Wave Representation in Atmospheric Models. Part II: Wave Intermittency Simulated with Convective Sources. *J. Atmos. Sci.*, *78*, 1339-1357. doi: 10.1175/JAS-D-20-0066.1

Kleinert, A., Friedl-Vallon, F., Guggenmoser, T., Höpfner, M., Neubert, T., Ribalda, R., … Preusse, P. (2014). Level 0 to 1 processing of the imaging fourier transform spectrometer GLORIA: generation of radiometrically and spectrally calibrated spectra. *Atmos. Meas. Tech.*, *7*(12), 4167-4184. doi: 10.5194/amt-7-4167-2014

Krasauskas, L., Ungermann, J., Ensmann, S., Krisch, I., Kretschmer, E., Preusse, P., & Riese, M. (2019). 3-d tomographic limb sounder retrieval techniques: irregular grids and laplacian regularisation. *Atmos. Meas. Tech.*, *12*(2), 853–872. Retrieved from https://www.atmos-meas-tech.net/12/853/2019/ doi: 10.5194/amt-12-853-2019

Krasauskas, L., Ungermann, J., Preusse, P., Friedl-Vallon, F., Zahn, A., Ziereis, H., … Riese, M. (2021). 3-d tomographic observations of rossby wave breaking over the north atlantic during the wise aircraft campaign in 2017. *Atmos. Chem. Phys.*, *21*(13), 10249–10272. doi: 10.5194/acp-21-10249-2021

Krisch, I., Ern, M., Hoffmann, L., Preusse, P., Strube, C., Ungermann, J., … Riese, M. (2020). Superposition of gravity waves with different propagation characteristics observed by airborne and space-borne infrared sounders. *Atmos. Chem. Phys.*, *20*(19), 11469–11490. Retrieved from https://acp.copernicus.org/articles/20/11469/2020/ doi: 10.5194/acp-20-11469-2020

Krisch, I., Preusse, P., Ungermann, J., Dörnbrack, A., Eckermann, S. D., Ern, M., … Riese, M. (2017). First tomographic observations of gravity waves by the infrared limb imager GLORIA. *Atmos. Chem. Phys.*, *17*(24), 14937–14953.

doi: 10.5194/acp-17-14937-2017

Krisch, I., Ungermann, J., Preusse, P., Kretschmer, E., & Riese, M. (2018). Limited angle tomography of mesoscale gravity waves by the infrared limb-sounder GLORIA. *Atmos. Meas. Tech.*, *11*(7), 4327–4344. Retrieved from `https://www.atmos-meas-tech.net/11/4327/2018/` doi: 10.5194/amt-11-4327-2018

Lang, S. T., Dawson, A., Diamantakis, M., Dueben, P., Hatfield, S., Leutbecher, M., ... Wedi, N. (2021). More accuracy with less precision. *Quart. J. Roy. Meteorol. Soc.*. (Accepted, In print) doi: 10.1002/qj.4181

Leighton, R., & Feynman, R. (1985). *"surely you're joking, Mr. Feynman!": Adventures of a curious character.* W. W. Norton.

Lighthill, M. J. (1978). Waves in fluids. *Cambridge University Press*, 504pp.

Lim, E., Hendon, H., Boschat, G., Hudson, D., Thompson, D., Dowdy, A., & Arblaster, J. (2019). Australian hot and dry extremes induced by weakenings of the stratospheric polar vortex. *Nature Geosci.*, *12*, 896-901. doi: 10.1038/s41561-019-0456-x

Marks, C. J., & Eckermann, S. D. (1995). A three-dimensional nonhydrostatic ray-tracing model for gravity waves: Formulation and preliminary results for the middle atmosphere. *J. Atmos. Sci.*, *52*(11), 1959-1984. doi: 10.1175/1520-0469(1995)052⟨1959:ATDNRT⟩2.0.CO;2

McLandress, C. (1998). On the importance of gravity waves in the middle atmosphere and their parameterization in general circulation models. *J. Atm. Sol.-Terr. Phys.*, *60*, 1357-1383. doi: 10.1016/S1364-6826(98)00061-3

McLandress, C., Shepherd, T. G., Polavarapu, S., & Beagley, S. R. (2012, MAR). Is Missing Orographic Gravity Wave Drag near 60 degrees S the Cause of the Stratospheric Zonal Wind Biases in Chemistry Climate Models? *J. Atmos. Sci.*, *69*(3), 802-818. doi: 10.1175/JAS-D-11-0159.1

Pitteway, M. L. V., & Hines, C. O. (1963). The viscous damping of atmospheric gravity waves. *Canadian Journal of Physics*, *41*(12), 1935-1948. doi: 10.1139/p63-194

Plougonven, R., de la Camara, A., Hertzog, A., & Lott, F. (2020, APR). How does knowledge of atmospheric gravity waves guide their parameterizations? *Quart. J. Roy. Meteorol. Soc.*, *146*(728, A), 1529-1543. doi: 10.1002/qj.3732

Polichtchouk, I., Shepherd, T., & Byrne, N. (2018, AUG 28). Impact of Parametrized Nonorographic Gravity Wave Drag on Stratosphere-Troposphere Coupling in the Northern and Southern Hemispheres. *Geophys. Res. Lett.*, *45*(16), 8612-8618. doi: 10.1029/2018GL078981

Polichtchouk, I., Shepherd, T., Hogan, R., & Bechtold, P. (2018, MAY). Sensitivity of the Brewer-Dobson Circulation and Polar Vortex Variability to Parameterized Nonorographic Gravity Wave Drag in a High-Resolution Atmospheric Model. *J. Atmos. Sci.*, *75*(5), 1525-1543. doi: 10.1175/JAS-D-17-0304.1

Preusse, P., Dörnbrack, A., Eckermann, S. D., Riese, M., Schaeler, B., Bacmeister, J. T., ... Grossmann, K. U. (2002). Space-based measurements of stratospheric mountain waves by CRISTA, 1. sensitivity, analysis method, and a case study. *J. Geophys. Res.*, *107(D23)*(8178). doi: 10.1029/2001JD000699

Preusse, P., Eckermann, S. D., Ern, M., Oberheide, J., Picard, R. H., Roble, R. G., ... Mlynczak, M. G. (2009). Global ray tracing simulations of the SABER gravity wave climatology. *J. Geophys. Res. Atmos.*, *114*. doi: 10.1029/2008JD011214

Rapp, M., Kaifler, B., Dörnbrack, A., Gisinger, S., Mixa, T., Reichert, R., ... Engel, A. (2021). SOUTHTRAC-GW: An Airborne Field Campaign to Explore Gravity Wave Dynamics at the World's Strongest Hotspot. *Bull. Amer. Meteor. Soc.*, *102*(4), E871 - E893. doi: 10.1175/BAMS-D-20-0034.1

Richter, J. H., Sassi, F., & Garcia, R. R. (2010). Toward a physically based gravity wave source parameterization in a general circulation model. *J. Atmos. Sci.*, *67*, 136-156.

Riese, M., Oelhaf, H., Preusse, P., Blank, J., Ern, M., Friedl-Vallon, F., ... Woiwode, W. (2014). Gimballed limb observer for radiance imaging of the atmosphere (GLORIA) scientific objectives. *Atmos. Meas. Tech.*, *7*(7), 1915-1928. doi: 10.5194/amt-7-1915-2014

Sakazaki, T., Fujiwara, M., & Shiotani, M. (2018). Representation of solar tides in the stratosphere and lower mesosphere in state-of-the-art reanalyses and in satellite observations. *Atmos. Chem. Phys.*, *18*, 1437-1456. doi: 10.5194/acp-18-1437-2018

Samtleben, N., Kuchař, A., Šácha, P., Pišoft, P., & Jacobi, C. (2020). Impact of local gravity wave forcing in the lower stratosphere on the polar vortex stability: effect of longitudinal displacement. *Ann. Geophys.*, *38*(1), 95–108. doi: 10.5194/angeo-38-95-2020

Sandu, I., Bechtold, P., Beljaars, A., Bozzo, A., Pithan, F., Shepherd, T. G., & Zadra, A. (2016, MAR). Impacts of parameterized orographic drag on the northern hemisphere winter circulation. *J. Adv. Model. Earth Syst.*, *8*(1), 196-211. doi: 10.1002/2015MS000564

Sato, K., Tateno, S., Watanabe, S., & Kawatani. (2012). Gravity wave characteristics in the Southern Hemisphere revealed by a high-resolution middle-atmosphere general circulation model. *J. Atmos. Sci.*, *69*, 1378-1396. doi: 10.1175/JAS-D-11-0101.1

Sato, K., Watanabe, S., Kawatani, Y., Tomikawa, Y., Miyazaki, K., & Takahashi, M. (2009, OCT 7). On the origins of mesospheric gravity waves. *Geophys. Res. Lett.*, *36*. doi: 10.1029/2009GL039908

Savitzky, A., & Golay, M. J. E. (1964). Smoothing and differentiation of data by simplified least squares procedures. *Analytical Chemistry*, *36*(8), 1627-1639. Retrieved from `http://dx.doi.org/10.1021/ac60214a047` doi: 10.1021/ac60214a047

Shen, X., Wang, L., & Osprey, S. (2020). tropospheric forcing of the 2019 Antarctic sudden stratospheric warming. *Geophys. Res. Lett.*, *47*, e2020GL089343. doi: 10.1029/2020GL089343

Strube, C., Ern, M., Preusse, P., & Riese, M. (2020). Removing spurious inertial instability signals from gravity wave temperature perturbations using spectral filtering methods. *Atmos. Meas. Tech.*, *13*(9), 4927–4945. Retrieved from `https://amt.copernicus.org/articles/13/4927/2020/` doi: 10.5194/amt-13-4927-2020

Strube, C., Preusse, P., Ern, M., & Riese, M. (2021). Propagation paths and source distributions of resolved gravity waves in ecmwf-ifs analysis fields around the southern polar night jet. *Atmos. Chem. Phys.*, *21*(24), 18641–18668. doi: 10.5194/acp-21-18641-2021

Torrence, C., & Compo, G. P. (1998). A practical guide to wavelet analysis. *Bull. Amer. Meteor. Soc.*, *79*(1), 61 - 78. doi: 10.1175/1520-0477(1998)079⟨0061:APGTWA⟩2.0.CO;2

Ungermann, J., Blank, J., Lotz, J., Leppkes, K., Hoffmann, L., Guggenmoser, T., ... Riese, M. (2011). A 3-D tomographic retrieval approach with advection compensation for the air-borne limb-imager GLORIA. *Atmos. Meas. Tech.*, *4*(11), 2509-2529. Retrieved from `http://www.atmos-meas-tech.net/4/2509/2011/` doi: 10.5194/amt-4-2509-2011

Ungermann, J., Kaufmann, M., Hoffmann, L., Preusse, P., Oelhaf, H., Friedl-Vallon, F., & Riese, M. (2010). Towards a 3-D tomographic retrieval for the airborne limb-imager GLORIA. *Atmos. Meas. Tech.*, *3*(6), 1647-1665. doi: 10.5194/amt-3-1647-2010

Van der Mescht, D., & Geldenhuys, M. (2019). Observations of mountain waves with interference generated by coastal mountains in south africa. *Meteorol. Appl.*, *26*, 409-415. doi: 10.1002/met.1771

Zhu, X. (1993, SEP 1). Radiative damping revisited - Parametrization of damping rate in the middle atmosphere. *J. Atmos. Sci.*, *50*(17), 3008-3021. doi: 10.1175/1520-0469(1993)050⟨3008:RDRPOD⟩2.0.CO;2

Zülicke, C., & Peters, D. (2006, DEC). Simulation of inertia-gravity waves in a poleward-breaking Rossby wave. *J. Atmos. Sci.*, *63*(12), 3253-3276. doi: 10.1175/JAS3805.1